




Atoms, dimers, and nanoparticles from orbital-free density-potential-functional theoryMartin-Isbjörn Trappe ^{1,*} William C. Witt ^{2,†} and Sergei Manzhos ^{3,‡}¹*Centre for Quantum Technologies, National University of Singapore, 3 Science Drive 2, Singapore 117543, Singapore*²*Department of Materials Science & Metallurgy, University of Cambridge, 27 Charles Babbage Road, Cambridge, CB3 0FS, United Kingdom*³*School of Materials and Chemical Technology, Tokyo Institute of Technology, Ookayama 2-12-1, Meguro-ku, Tokyo 152-8552, Japan*

(Received 19 April 2023; revised 18 October 2023; accepted 14 November 2023; published 1 December 2023)

Density-potential-functional theory (DPFT) is an alternative formulation of orbital-free density functional theory that may be suitable for modeling the electronic structure of large systems. To date, DPFT has been applied mainly to quantum gases in one- and two-dimensional settings. In this work, we study the performance of DPFT when applied to real-life systems: atoms, dimers, and nanoparticles. We build on systematic Suzuki-Trotter factorizations of the quantum-mechanical propagator and on the Wigner function formalism, respectively, to derive nonlocal as well as semilocal functional approximations in complete analogy to their well-established lower-dimensional versions, without resorting to system-specific approximations or *ad hoc* measures of any kind. The cost for computing the associated semiclassical ground-state single-particle density scales (quasi)linearly with particle number. We illustrate that the developed density formulas become relatively more accurate for larger particle numbers, can be improved systematically, are quite universally applicable, and, hence, may offer alternatives to existing orbital-free methods for mesoscopic quantum systems.

DOI: [10.1103/PhysRevA.108.062802](https://doi.org/10.1103/PhysRevA.108.062802)**I. INTRODUCTION**

Electronic structure calculations form the theoretical basis of today's materials science and chemistry, where demand for reliable predictions of electronic energies and electron distributions has been growing steadily for decades [1–6]. The majority of applications rely on Kohn-Sham density functional theory (KS-DFT) [2], which self-consistently builds the spatial electron density distribution n and the associated energy $E[n]$ from orbitals of an auxiliary, effectively noninteracting system. Since these orbitals have to be mutually orthogonal, the computational cost of standard KS-DFT scales cubically with the electron number N . Consequently, high-throughput KS calculations are typically limited to a few hundred atoms, although linear-scaling implementations can target much larger particle numbers, commonly achieved through localized orbitals and massive parallelization [7–12]. However, these computationally efficient approaches rely on known or presupposed properties of the target systems and are not easily transferable beyond the class of systems they are designed for [13].

A tradeoff among scalability, accuracy, and transferability is unavoidable. With emphasis on efficiency for large N , orbital-free density functional theory (OF-DFT) naturally becomes the electronic structure method of choice for routinely investigating thousands to millions of interacting particles [14,15], without relying on particular approximations from the outset like, for example, in the density

functional tight-binding method [16]. OF-DFT is the original (Hohenberg-Kohn) formulation of DFT, which has been in the shadows for decades due to the absence of accurate enough functionals for the kinetic energy. Today, however, the field of OF-DFT is enjoying rapid growth due to a constellation of factors that include advanced computational tools, such as modern optimizers and machine learning [17–21], as well as new theoretical developments [22–29].

OF-DFT primarily aims at utilizing efficient and accurate functionals for the kinetic energy E_{kin} since (i) other major contributions to the total energy, such as the electron-ion or Hartree energy, are known and (ii) a generic exchange-correlation energy functional such as PBE [30,31] can be accurate enough for many OF-DFT studies of electronic systems in three dimensions (3D). Importantly, we note that DFT implementations are less developed for lower-dimensional settings and non-Coulombic interactions, not least due to the focus on 3D electronic systems ultimately required for chemistry and materials applications. For example, exchange-correlation functionals for two-dimensional (2D) electronic systems have been rigorously derived only in recent history [32]. Moreover, some highly accurate approximations cannot be extended beyond one-dimensional (1D) geometries [33,34], and the interactions in ultracold Fermi gases demand DFT techniques that deviate markedly from traditional routes [35–38]. While functionals for 3D are needed in the vast majority of use cases, we speculate that the most transferable functionals will extend seamlessly into low-dimensional settings, and that the development of functionals for 3D will benefit from lessons learned with tractable systems in 1D and 2D.

Much of scholarly material on OF-DFT features approximations of the kinetic energy *density* functional $E_{\text{kin}}[n]$

*Corresponding author: martin.trappe@quantumlah.org†wcw28@cam.ac.uk‡manzhos.s.aa@m.titech.ac.jp

(KEDF), for which even the general noninteracting version is not known explicitly (in position-space representation). The following selection of OF-DFT approaches provides an overview pertinent to this work, but is by no means complete; see Refs. [15,39] and references therein for broader surveys. Practical implementations of OF-DFT are accessible through software packages like GPAW [40], PROFESS [41,42], ATLAS [39,43,44], CONUNDRUM [45], and DFTPY [25], which build on nonlocal and semilocal KEDFs that prove appropriate for certain classes of systems. In contrast to rudimentary approximations such as the prototypical Thomas-Fermi (TF) model, nonlocal KEDFs are capable of producing the typical oscillations of quantum-mechanical densities that can be viewed as aggregations of many KS-type single-particle densities. But these accurate functionals are limited mainly to main group metals with inroads into bulk semiconductors [46–49]. Moreover, their application commonly depends on the average density in the unit cell, such that addressing isolated systems remains problematic [50], although efforts are made to overcome these shortcomings, for example, through a KEDF [39] that is inspired by the local density approximation (LDA). Alternatively, rigorous expansions in terms of the density gradient have been considered [51–53], but technical difficulties in adequately resumming higher-order terms of this asymptotic series for obtaining systematic and, hence, maximally transferable KEDFs have impeded widespread application, though very accurate gradient expansions can be constructed for special cases in 1D [54]. The truncation of the gradient expansion renders corresponding KEDFs valid only in regions of slowly varying density, a feature shared with modern semilocal KEDFs that incorporates the gradient and Laplacian of the density [50,55–57]. But some of these functionals, which specifically target electronic systems in 3D, are of limited use for regions of highly variable density. Furthermore, gradient-expanded KEDFs that improve upon the TF and von-Weizsäcker (vW) KEDFs [53] are commonly (i) parametrized in an *ad hoc* fashion and fitted to existing data like in [58] or (ii) take into account constraints that only apply to 3D electronic matter [59,60]. Specific combinations of nonlocal and semilocal terms have been explored, for example, such that a number of exact constraints are met upon optimizing free parameters [61,62]. KEDFs can also be constructed directly from models of the one-body reduced density matrix for electronic systems [63]. Some OF-DFT variants achieve accuracy and efficiency through electron densities restricted to families of functions for the constituting atoms, partitioning of the target system, and other *ad hoc* measures. Applications of OF-DFT can also benefit from problem-specific machine-learned functionals, some of which deliver chemical accuracy, though general-purpose functionals have yet to materialize [17,18,64–66]. The kinetic as well as total energy can also be expressed in terms of the external potential, which is bijectively related to the particle density. In the resulting potential functional theories [67,68], both the kinetic energy in general and gradient expansions in particular are accessible more naturally than in DFT. However, the according OF-DFT implementations have so far improved upon TF-type models only for selected systems, and extensions to 3D prove difficult [68–70].

In summary, the fundamental importance of the quantum many-body problem across scientific branches and the difficulty in finding general-purpose solutions have motivated a multitude of approaches to OF-DFT that predominantly target electronic structure calculations. Although each of these methods presents a viable route to address specific sets of issues, none offers a clear path of *systematic and nonempirical* improvement *toward* the exact energy functional across virtually all fermion systems, that is, across dimensions, type of interactions, number of fermion species, boundary conditions, and for observables in momentum as well as in position space. Such a universal orbital-free methodology would allow us to transfer lessons learned in studying very disparate systems and would enjoy widespread application if demands on accuracy and computational efficiency are met. This work features density-potential-functional theory (DPFT), which promises to deliver such a unified, parameter-free framework for practically relevant applications.

The conception of DPFT by Schwinger and Englert dates back to the early 1980s, with a series of works that developed the semiclassical atom [71–80]; see Ref. [81] for a review of these early developments, which relied on the properties of the central nuclear potential and cannot easily be transferred to molecules and materials. The basis of DPFT is an exact bifunctional for the total energy that depends on (i) the particle density n and (ii) an effective potential V that merges the external potential with the interaction effects. The kinetic energy in DPFT is expressed through the Legendre transform of the KEDF. In reformulating the Hohenberg-Kohn energy functional, this procedure yields an explicit expression for the noninteracting kinetic energy functional in terms of V , permits systematic approximations, and thereby alleviates the need of searching for approximations of the unknown $E_{\text{kin}}[n]$. DPFT has been applied to (i) noninteracting systems for benchmarking purposes [36,37,82,83], (ii) systems in one [83], two [36–38,84], and three [82] dimensions, (iii) small [38,82,83] and large [37,38,83,84] particle numbers, (iv) graphene heterostructures [84], (v) single atoms [71–80], and (vi) interacting Fermi gases [36,38,85]. The unifying feature of all these applications is the systematic, parameter-free methodology of the DPFT approximations. In fact, the core principles of DPFT have permeated beyond physics: Ref. [86] offers a unified theory for ecology based on the mathematical structure of DPFT. Aside from DPFT implementations aimed at periodic systems, an important missing element in this array of applications is the calculation of electronic structure.

This work establishes an avenue for electronic structure calculations of isolated systems based on semiclassical approximations for DPFT. We employ two disjunct schemes that feature nonlocal and semilocal approximations, respectively. First, we (i) utilize the formulas for quantum-corrected densities derived in Ref. [82], where Suzuki-Trotter factorizations of the time-evolution operator produce a hierarchy of systematic improvements upon the TF approximation without a gradient expansion, and (ii) derive the kinetic energy through an accordingly approximated one-body density matrix. In extending this approach to finite temperature, we reduce the computational cost of the quantum-corrected densities to quasilinear scaling. The second approximation scheme builds

on the Wigner function formalism and delivers semilocal, linearly scaling formulas for densities and energies through “Airy-averaged” gradient expansions that address evanescent regions accurately and efficiently across dimensions. Here, we derive the expressions for densities and energies for 3D systems, in complete analogy to the 1D and 2D settings that are covered in Refs. [38,83] and [36–38], respectively. Our primary objective is the proof-of-principle applicability of these two DPFT approximation schemes to electronic structure problems. We show that even the next-to-leading-order semiclassical DPFT densities improve significantly upon their lowest order (the TF density) and approach the quality of KS densities as the particle number becomes large. Unfortunately, while some modern KS exchange-correlation functionals sacrifice accuracy of densities in favor of accurate total energies [87], the reverse seems to hold for the DPFT approximations used in this work: We find the improvements of total energies (as well as energy differences, which matter ultimately) over the TF energies to be minor in practice, although the improvements are sufficient to bind H_2 , an outcome that cannot be obtained from a self-consistent TF calculation.

In this work we study the applicability of DPFT approximation schemes to real-life electronic structure. The test cases range from single atoms to relatively large (by *ab initio* standards) nanoparticles. Although the semiclassical DPFT approximations are expected to become relatively accurate only for large particle numbers, we will calculate atomic densities and dimer properties. These preparatory calculations will help establish the reliability of our approximation schemes for mesoscopic nanoparticles. Metal nanoparticles composed of $\sim 10\text{--}10^6$ atoms, are an important active area of research that fuels modern technologies, including photovoltaics, catalysis, and drug delivery [39,88–92], in particular because the large ratio between surface and bulk atoms in metal nanoparticles yields unique and useful mechanical, chemical, optical, and electrical properties that differ markedly from their solid-state versions. In isolated systems like metal nanoparticles, the electron density easily drops 10 orders of magnitude within angstroms when crossing the evanescent region from the bulk on the way to vacuum. Such inhomogeneities require special care, as discussed, for example, in Ref. [93], where accurate OF-DFT densities and energies are reported based on an LDA-inspired KEDF. Comprehensive KS analyses of more exotic metal nanoparticles have only recently become possible and are commonly combined with advanced global optimization techniques that deliver the low-energy nanoparticle configurations [91,94,95]. For example, geometries of a gold-copper nanoalloy composed of just over 300 atoms are found with a genetic algorithm in Ref. [96]. Disregarding stringent demands on accuracy and transferability, the issue of computational cost can likely be resolved with modern OF-DFT implementations [97]: A refined periodic code that can process any KEDFs recently produced the electronic structure of a (1×10^6) -atom Al-nanoparticle on a single CPU [25], but, of course, such impressive outcomes inherit the shortcomings of the underlying KEDFs.

This work is organized as follows. In Sec. II we introduce the method of orbital-free DPFT. Section II A recapitulates the general DPFT formalism, subsequently supplemented

with systematic semiclassical approximations that derive from Suzuki-Trotter factorizations (Sec. II B) and approximate Wigner functions (Sec. II C), respectively. In Sec. III we detail our numerics, such as the pseudopotentials we use for valence- and all-electron calculations. In Sec. IV, we present our main results for the electronic structure of atoms (Sec. IV A), dimers (Sec. IV B), and nanoparticles (Sec. IV C). We conclude in Sec. V with the wider implications of this work and its potentially fruitful extensions. In the Appendixes we collect details on our numerical procedures and on the derivations of the approximate DPFT functionals of energy and density for three-dimensional settings as introduced in Secs. II B and II C.

II. DENSITY-POTENTIAL-FUNCTIONAL THEORY FOR ELECTRONIC STRUCTURE

The computational cost of OF-DFT is not explicitly dependent on the particle number. But in practice, and in particular for electronic structure, an N dependence is introduced via numerical integration grids that have to be large enough for sufficiently converging densities and energies. A moderate grid size can be adequate even for millions of particles, for example, for some interacting ultracold atomic gases, whereas electronic structure calculations demand an adequate sampling of the electron distribution around *each* nucleus, which makes the OF-DFT approach scale with the number of atoms or number N of electrons, with the proviso that the employed KEDFs are efficient enough, comparable to the TF-KEDF in the best case. The latter holds for many semilocal functionals, while nonlocal KEDFs incur costs that scale at least like $N \ln N$. Furthermore, all that holds only if the cost of the interaction functional is small enough; a lower bound is usually put in place by the Hartree energy that scales like $N \ln N$. The main purpose of this work is to introduce two disjunct semiclassical DPFT approximations whose computational costs for electronic structure calculations scale like N and $N \ln N$, respectively.

A. General formalism of density-potential-functional theory

Orbital-free density functional theory (OF-DFT) seeks the extremum of the constrained density functional of the total energy

$$E = E[n, \mu] = E_{\text{kin}}[n] + E_{\text{ext}}[n] + E_{\text{int}}[n] + \mu \left(N - \int (\mathbf{dr}) n(\mathbf{r}) \right), \quad (1)$$

which sums the kinetic energy, the energy due to the single-particle external potential, and the interaction energy for a quantum system of N particles, associated with the chemical potential μ . DPFT introduces the effective potential energy

$$V(\mathbf{r}) = \mu - \frac{\delta E_{\text{kin}}[n]}{\delta n(\mathbf{r})}, \quad (2)$$

such that the Legendre transform

$$E_1[V - \mu] = E_{\text{kin}}[n] + \int (\mathbf{dr}) (V(\mathbf{r}) - \mu) n(\mathbf{r}) \quad (3)$$

of the kinetic energy functional $E_{\text{kin}}[n]$ yields

$$E = E[V, n, \mu] = E_1[V - \mu] - \int (d\mathbf{r}) n(\mathbf{r}) (V(\mathbf{r}) - V_{\text{ext}}(\mathbf{r})) + E_{\text{int}}[n] + \mu N. \quad (4)$$

The V and n variations at the stationary point of $E[V, n, \mu]$ obey

$$\delta V : n[V - \mu](\mathbf{r}) = \frac{\delta E_1[V - \mu]}{\delta V(\mathbf{r})} \quad (5)$$

and

$$\delta n : V[n](\mathbf{r}) = V_{\text{ext}}(\mathbf{r}) + \frac{\delta E_{\text{int}}[n]}{\delta n(\mathbf{r})}, \quad (6)$$

respectively. The μ variation, combined with Eq. (5), reproduces the particle-number constraint

$$\int (d\mathbf{r}) n(\mathbf{r}) = N. \quad (7)$$

Equation (5) yields the particle density for any given μ and effective potential, e.g., the noninteracting density in the noninteracting case ($V = V_{\text{ext}}$). We find candidates of the ground-state density from the self-consistent solution of Eqs. (5)–(7) for a given interaction functional $E_{\text{int}}[n]$. The fundamental variables of DPFT are V and n , in contrast both to the standard Hohenberg-Kohn DFT and to potential functional theory [68,69], although the optimized effective potential approach to OF-DFT is related in spirit to DPFT (see Ref. [69] and references therein). In the following, we reiterate only the most important features and formulas of DPFT pertinent to this work; details on DPFT can be found in Refs. [36–38,77,79,83].

The main advantage of orbital-free DPFT is to avoid the not explicitly known density functional $E_{\text{kin}}[n]$ of the kinetic energy in favor of its Legendre transform

$$E_1[V - \mu] = \text{tr}\{\mathcal{E}_T(H - \mu)\}. \quad (8)$$

Here, $H = H(\mathbf{R}, \mathbf{P})$ is the Hamiltonian of a system (at finite or zero temperature T), for which we may neglect couplings between the position operator \mathbf{R} and the momentum operator \mathbf{P} , for example, of spin-orbit type [37,38,79]. The single-particle trace in Eq. (8) includes a degeneracy factor g , which can, for example, encode spin multiplicity. We will use the explicitly known noninteracting version

$$\mathcal{E}_T^{(0)}(A = H - \mu) = (-k_B T) \ln(1 + e^{-A/k_B T}) \quad (9)$$

of \mathcal{E}_T , which has a strong track record also for interacting systems [36–38,77,79,82,83], akin to neglecting the interacting part of the kinetic energy in constructions of the KS exchange-correlation functionals. Here and in the following we omit arguments of functions for brevity whenever expedient.

Equations (8) and (9) permit explicit systematic approximations. In the following, we introduce two independent semiclassical schemes for DPFT. They can be benchmarked unambiguously for noninteracting systems or if the interaction functional is known or prescribed.

B. Densities and energies from Suzuki-Trotter factorizations

As derived in Refs. [38,82], Eqs. (5) and (8) at $T = 0$ yield

$$n(\mathbf{r}) = g \langle \mathbf{r} | \eta(\mu - H) | \mathbf{r} \rangle = g \int \frac{dt}{2\pi i t} \underset{\text{clockwise}}{\curvearrowright} e^{\frac{i}{\hbar} \mu t} \langle \mathbf{r} | U(t) | \mathbf{r} \rangle. \quad (10)$$

Here, we make use of the Fourier transform of the step function $\eta(\dots)$, and the integration path from $t = -\infty$ to $t = \infty$ crosses the imaginary t axis in the lower half-plane. Application-specific versions of Eq. (10) can be derived. For example, linear dispersion [instead of the single-particle kinetic-energy operator $T = \mathbf{P}^2/(2m)$] in Ref. [84] accounts for the Dirac cone in graphene, and momental densities are immediately accessible through the momentum-space version $n(\mathbf{p}) = g \langle \mathbf{p} | \eta(\mu - H) | \mathbf{p} \rangle$ of Eq. (10). In any case, the time-evolution operator $U(t) = e^{-\frac{i}{\hbar} H t}$ with Hamiltonian $H = T + V$ in Eq. (10) can be systematically approximated by tailored Suzuki-Trotter factorizations. The crudest approximation of that sort is $U \approx e^{-\frac{i}{\hbar} T t} e^{-\frac{i}{\hbar} V t}$, which yields the TF density

$$n_{\text{TF}}(\mathbf{r}) = \frac{g \Omega_D}{D (2\pi \hbar)^D} [2m(\mu - V(\mathbf{r}))]_+^{D/2} = \frac{g \Omega_D}{D (2\pi \mathcal{U}^2)^D} [2(\mu - V(\mathbf{r}))]_+^{D/2}, \quad (11)$$

with $[z]_+ = z \eta(z)$ and the solid angle Ω_D in D dimensions. Equation (11) exposes the units of energy (\mathcal{E}) and length (\mathcal{L}) via the dimensionless (mass-dependent) constant $\mathcal{U} = \hbar^2/(m \mathcal{L}^2 \mathcal{E})$. In all formulas of this work that exhibit \mathcal{U} , the quantities of energy are given in units of \mathcal{E} and those of length in units of \mathcal{L} . For example, μ in Eq. (11) is implicit for μ/\mathcal{E} , and $n_{\text{TF}}(\mathbf{r})$ comes in units of \mathcal{L}^{-D} . For the concrete examples in the sections below we use units of $\mathcal{E} = \text{eV}$ and $\mathcal{L} = \text{\AA}$ and choose the electron mass for m , such that $\mathcal{U} \approx 7.61996$. Harmonic oscillator units, for instance, are implemented by $\mathcal{U} = 1$.

In this work, we transform the approximation

$$n_{3'}(\mathbf{r}) = g \int (d\mathbf{a}) \left(\frac{k_{3'}}{2\pi a} \right)^D J_D(2a k_{3'}) \quad (12)$$

for the single-particle density into computationally more feasible expressions. Equation (12) is the quantum-corrected successor of n_{TF} [38,82], with the Bessel function $J_D(\dots)$ of order D and the effective Fermi wave number $k_{3'} = \frac{1}{\hbar} \{2m[\mu - V(\mathbf{r} + \mathbf{a})]\}_+^{1/2}$. In contrast to the local TF density, whose computational cost scales with size G of the numerical grid, $n_{3'}(\mathbf{r})$ is a fully nonlocal expression, which samples the effective potential V in a neighborhood of the position \mathbf{r} , such that its computational cost scales like G^2 . The accuracy of $n_{3'}$ and its associated kinetic energy

$$E_{\text{kin}}^{(3')} = \frac{g \Omega_D}{(2\pi \mathcal{U}^2)^D (2D + 4)} \int (d\mathbf{r}) \{2[\mu - V(\mathbf{r})]\}_+^{\frac{D+2}{2}} \quad (13)$$

are sufficient for qualitative modeling of some basic chemistry applications like bond making and breaking. While such a ca-

capacity for small molecules is a clear improvement over the TF approximation, n_{3^f} should become quantitatively competitive with KS only for larger particle numbers.

$$n_{3^f}^{\mathcal{F}}(\mathbf{r}) = \frac{g \Omega_D}{D (2\pi)^D} \mathcal{F}^{-1} \left\{ \int (d\mathbf{r}') e^{-i\mathbf{k}\mathbf{r}'} \left[\frac{2}{\mathcal{U}} [\mu - V(\mathbf{r}')] - \frac{\mathbf{k}^2}{4} \right]_+^{D/2} \right\}(\mathbf{r}). \quad (14)$$

In Appendix A (see also Ref. [38]), which expresses n_{3^f} in terms of Fourier transforms $\mathcal{F}\{\dots\}$ and is more efficient than Eq. (12), although the computational cost of $n_{3^f}^{\mathcal{F}}$ still scales like G^2 . In Appendix A we also derive the finite-temperature version

$$n_{3^f}^T(\mathbf{r}) = \frac{g}{\Gamma[D/2]} \left(\frac{k_B T}{2\pi \mathcal{U}} \right)^{D/2} \times \int_0^\infty dy \mathcal{F}^{-1} \{ \mathcal{F} \{ f_y(\mathbf{r}') \}(\mathbf{k}) g_y^D(k) \}(\mathbf{r}), \quad (15)$$

whose cost scales like $G \ln G$ thanks to fast Fourier transforms (see Appendix A), albeit with a (potentially) large prefactor that tends to increase with decreasing temperature. Here, $\Gamma(\dots)$ denotes the gamma function,

$$f_y(\mathbf{r}') = \exp\{[\mu - V(\mathbf{r}')]/(k_B T)\} - y \exp\{[\mu - V(\mathbf{r}')]/(k_B T)\}, \quad (16)$$

and

$$g_y^D(k) = \int_0^\infty dx x^{D/2-1} \exp[-y \exp(x + \kappa)] \quad (17)$$

is easily tabulated for all required values of $\kappa = (\hbar k)^2/(8m k_B T) = \mathcal{U} k^2/(k_B T)$, where k is the magnitude of the wave vector \mathbf{k} in Fourier space. With small enough temperature, $n_{3^f}^T$ can be used in lieu of the ground-state density n_{3^f} .

C. Airy-averaged densities and energies

From Refs. [36,37,83], we recapitulate the most important expressions of our second approximation scheme, which derives from representing the trace in Eq. (8) by the classical phase space integral

$$\text{tr}\{\mathcal{E}_T(A(\mathbf{R}, \mathbf{P}))\} = g \int \frac{(d\mathbf{r})(d\mathbf{p})}{(2\pi \hbar)^D} [\mathcal{E}_T(A)]_w(\mathbf{r}, \mathbf{p}). \quad (18)$$

Equation (12) is efficient enough for the calculation of isotropic densities. For anisotropic densities at zero temperature, we provide

The momentum integral over the Wigner function $[\mathcal{E}_T(A)]_w$ of $\mathcal{E}_T(A)$ can be approximated by

$$\int (d\mathbf{p}) [\mathcal{E}_T(A)]_w(\mathbf{r}, \mathbf{p}) \cong \int (d\mathbf{p}) \left\langle \mathcal{E}_T(\tilde{A}_w) - \frac{\hbar^2 (\nabla^2 V)}{12m} \mathcal{E}_T''(\tilde{A}_w) \right\rangle_{\text{Ai}}. \quad (19)$$

Here, $\tilde{A}_w(\mathbf{r}, \mathbf{p}) = H_w(\mathbf{r}, \mathbf{p}) - \mu - x a(\mathbf{r})$, with the Wigner function $H_w(\mathbf{r}, \mathbf{p}) = \mathbf{p}^2/(2m) + V(\mathbf{r})$ of the single-particle Hamiltonian and $a(\mathbf{r}) = |\hbar \nabla V(\mathbf{r})|^{2/3}/(2m^{1/3})$. We also call $\langle f \rangle_{\text{Ai}} = \int_{-\infty}^\infty dx \text{Ai}(x) f(x)$, with the Airy function $\text{Ai}(\dots)$, the Airy average of the function f , and “ \cong ” stands for an approximation that reproduces the leading gradient correction exactly. Equation (19) holds not only for $\mathcal{E}_T(A)$, but for any function of A that has a Fourier transform. Equation (19) is exact up to the leading gradient correction $[O(\nabla^2)]$, and thus presents a systematic correction to the TF approximation, which is recovered in the uniform limit $[O(\nabla^0)]$. However, the “Airy average” in Eq. (19) also contains higher-order gradient corrections that enter through the Moyal products from the power-series expansion of $\mathcal{E}_T(A)$ in Eq. (18). These higher-order corrections are responsible for the almost exact behavior of particle densities across the boundary between classically allowed and forbidden regions, where the TF approximation can fail epically (even if supplemented with the leading gradient correction [37]). Eventually, we obtain the Airy-averaged particle densities for one-, two-, and three-dimensional geometries by combining Eqs. (5), (8), (9), (18), and (19) and by evaluating the momentum integral of Eq. (19). The 1D and 2D situations are covered extensively in Refs. [83] and [36,37], respectively. Here, we derive the explicit Airy-averaged expressions for energies and densities in 3D.

The Airy-averaged 2D ground-state densities $n_{\text{Ai}}^{T=0}$ of Ref. [37] exhibit unphysical oscillations in the vicinity of positions \mathbf{r} where $\nabla V(\mathbf{r}) = 0$. By introducing a small but finite temperature T , we obtain densities that are well behaved everywhere. The analogous derivation of the finite-temperature 3D expression

$$n_{\text{Ai}}^T(\mathbf{r}) = u_0 \times \begin{cases} \frac{a(\mathbf{r})}{k_B T} \int dx \mathcal{A}(x) [u_1 \text{Li}_{1/2}(-e^{-v_x(\mathbf{r})}) + u_2(\mathbf{r}) \text{Li}_{-3/2}(-e^{-v_x(\mathbf{r})})], & a(\mathbf{r}) > 0 \\ u_1 \text{Li}_{1/2}(-e^{-v_0(\mathbf{r})}) + u_2(\mathbf{r}) \text{Li}_{-3/2}(-e^{-v_0(\mathbf{r})}), & a(\mathbf{r}) = 0 \end{cases} \quad (20)$$

and details of its numerical implementation are provided in Appendix A. We denote the polylogarithm of order s by $\text{Li}_s(\dots)$ and the negative antideriva-

tive of the Airy function by $\mathcal{A}(x) = \int_x^\infty dy \text{Ai}(y)$. We set $\mathcal{A}(x) = 0$ for $x > 100$, use the asymptotic approximation $\mathcal{A}(x) \approx 1 - \cos[\pi/4 + (2/3)|x|^{3/2}]/(\sqrt{\pi}|x|^{3/4})$ for

$x < -150$, and tabulate $\mathcal{A}(x)$ for $-150 \leq x \leq 100$. We have

$$u_0 = -\frac{g}{(2\pi)^{3/2}}, \quad (21)$$

$$u_1 = \left(\frac{k_B T}{\mathcal{U}}\right)^{3/2}, \quad (22)$$

$$u_2(\mathbf{r}) = -\frac{\Delta V(\mathbf{r})}{12} \left(\frac{k_B T}{\mathcal{U}}\right)^{1/2}, \quad (23)$$

and

$$v_x(\mathbf{r}) = \frac{1}{k_B T} [V(\mathbf{r}) - \mu - x a(\mathbf{r})]. \quad (24)$$

In Appendix A we also derive $E_1^{\text{Ai},T}[V - \mu]$ and the corresponding value

$$E_{\text{kin}}^{\text{Ai},T} = E_1^{\text{Ai},T}[V - \mu] - \int (d\mathbf{r}) V(\mathbf{r}) n_{\text{Ai}}^T(\mathbf{r}) + \mu N \quad (25)$$

of the Airy-averaged kinetic energy at the stationary point of E . However, the ground-state kinetic energy

$$\begin{aligned} E_{\text{kin}}^{\text{Ai}} &= \frac{g}{(2\pi\hbar)^3} \int (d\mathbf{r}) \left\langle 4\pi \int dp \frac{p^4}{2m} \left[f(\tilde{A}_W) - \frac{\hbar^2 (\nabla^2 V)}{18m} f''(\tilde{A}_W) \right] \right\rangle_{\text{Ai}} \\ &= \frac{g}{4\pi^2 \mathcal{U}^2} \int (d\mathbf{r}) \left\{ \int_0^\infty dx \text{Ai}\left(x + \frac{V-\mu}{a}\right) \left[\frac{\sqrt{\mathcal{U}}}{5} (2ax)^{5/2} - \frac{\mathcal{U}^{3/2} (\nabla^2 V)}{6} (2ax)^{1/2} \right], a(\mathbf{r}) > 0 \right. \\ &\quad \left. \left[\frac{\sqrt{\mathcal{U}}}{5} [2(\mu - V)]_+^{5/2} - \frac{\mathcal{U}^{3/2} (\nabla^2 V)}{6} [2(\mu - V)]_+^{1/2} \right], a(\mathbf{r}) = 0 \right\} \end{aligned} \quad (26)$$

is much better behaved numerically than $E_{\text{kin}}^{\text{Ai},T}$, such that we utilize $E_{\text{kin}}^{\text{Ai}}$ for calculating the DPFT energies also for systems at finite temperature as long as T is small enough. We obtain Eq. (26) after suitable integrations by part and evaluation of the momentum integral in

$$\begin{aligned} E_{\text{kin}} &= \text{tr}\{T \eta(\mu - H)\} \\ &= \frac{g}{(2\pi\hbar)^3} \int (d\mathbf{r}) \int (d\mathbf{p}) \frac{\mathbf{p}^2}{2m} [f(A)]_W(\mathbf{r}, \mathbf{p}) \\ &\cong E_{\text{kin}}^{\text{Ai}} = \frac{g}{(2\pi\hbar)^3} \int (d\mathbf{r}) \int (d\mathbf{p}) \frac{\mathbf{p}^2}{2m} \\ &\quad \times \int dx \text{Ai}(x) \left[f(\tilde{A}_W) - \frac{\hbar^2 (\nabla^2 V)}{12m} \frac{D-1}{D} f''(\tilde{A}_W) \right], \end{aligned} \quad (27)$$

reported in Ref. [37], for $f(A) = \eta(-A)$, $f''(A) = \delta'(-A)$, and $D = 3$. For constant effective potential V (then, $a = 0$), Eq. (26) recovers the TF kinetic energy [cf. Eq. (13)]. Like in the 2D case, $E_{\text{kin}}^{\text{Ai}}$ does not suffer from unphysical oscillations as $a \rightarrow 0$. The computational costs of n_{Ai}^T , E_1^{Ai} , and $E_1^{\text{Ai},T}$ all scale with grid size G (and thus linearly with particle number N for electronic matter), just like the TF approximation, but in the current implementation the prefactor due to the Airy average usually comes in at about 10^3 – 10^5 for high-precision calculations.

III. NUCLEAR BACKGROUND, INTERACTION ENERGIES, AND NUMERICS

For the nuclear Coulomb potential, n_3 diverges logarithmically, like $\ln(1/r)$ as $r \rightarrow 0$, a stark improvement upon the $r^{-3/2}$ scaling of n_{TF} . This observation and the scaling behavior of n_{Ai}^T will be covered in detail elsewhere. Our numerical studies suggest that n_{Ai}^T diverges like n_{TF} at singularities of the (effective) potential, which is not surprising since n_{Ai}^T is a gradient expansion built on n_{TF} as the leading term. When employing the semiclassical densities introduced here, we

therefore have to replace the nuclei's Coulomb potentials by pseudopotentials. Alternative DFT formulations that can cope with unregularized singular potentials, for example, via proper incorporation of the Scott correction [77,98] or suitable basis function expansions are currently being developed [99,100]. For all-electron calculations we replace the bare Coulomb potential of a nucleus of charge Z by the smooth function

$$\begin{aligned} \mathcal{A}_\alpha^{(Z)}(r) &= -ZW \left((0.923 + 1.568\alpha) \exp[-(0.241 \right. \\ &\quad \left. + 1.405\alpha)^2 r^2] + \frac{\text{Erf}(\alpha r)}{r} \right), \end{aligned} \quad (28)$$

which recovers the Coulomb potential for $\alpha \rightarrow \infty$ (see Ref. [101]). Of course, other replacements of the ionic Coulomb potential are possible [102], but Eq. (28) suffices for the proof-of-principle calculations in this work. We have $W = \mathcal{U} \tilde{A}/a_0 \approx 14.39965$, with Bohr radius a_0 , dimensionless upon expressing all quantities of length in \AA and all energies in eV. $\text{Erf}(\dots)$ denotes the error function. By demanding $\mathcal{A}_\alpha^{(Z)}(0) = -2ZW/\Delta x$, where Δx is the lattice constant of the numerical grid, we determine an appropriate value of α . This condition is implied by the most simple regularization

$$\mathcal{C}^{(Z)}(r) = -\frac{ZW}{\max\{r, \Delta x/2\}} \quad (29)$$

of the Coulomb potential, which coincides with $-ZW/r$ (except at the origin) and is smooth at $r = \Delta x$. For calculating valence densities with two (three) electrons per Mg (Al) atom we enlist the GGA pseudopotentials that accompany the OF-DFT package PROFESS [41,42]. In all our calculations we treat all electrons as unpolarized (also systems with an odd number of electrons); hence, $g = 2$.

Approximations of the interaction functionals and their derivatives in Eq.(6) can, in principle, be obtained consistently within the same approximation schemes that yield the semiclassical approximations of Eq. (5). This agenda is beyond the scope of this article, but the structural similarity

between DPFT and KS-DFT invites the use of established KS exchange-correlation functionals for calculating Coulomb-interacting systems in 3D with DPFT. For the DPFT calculations in this work we used the LDA [103] and PBE [30,31] implementations from the LIBXC library [104]. We emphasize that our DPFT results do not take as input any results of KS calculations.

The KS-DFT calculations for comparing with the DPFT results were performed in GAUSSIAN 16 [105] and in ABINIT [106]. We used the $6-31g(d,p)$ basis set for atoms and dimers and D95 for the 201-atom Al nanoparticle. Gaussian were done with LSDA [103,107] and PBE functionals. All ABINIT calculations were performed with PBE, a plane-wave cutoff of 500 eV, and local pseudopotentials from [108,109]. In ABINIT, the systems were placed in a large vacuum box (e.g., 36 \AA^3 for the nanoparticle), and the calculations done at the gamma point. Coupled-cluster calculations for atoms were performed in GAUSSIAN 16 with singles, doubles, and perturbative triples [CCSD(T)], using the *aug-cc-pv5z* basis set.

To compare with conventional OF-DFT approaches, we calculated the valence densities of the atoms and dimers with PROFESS based on (i) the standard second-order gradient expansion of the kinetic energy functional [53] and (ii) the Pauli-Gaussian kinetic energy functional PGSL β [56] with $\beta = 0.25$. We additionally attempted the nanoparticle with both approaches, but only achieved a converged result with the gradient expansion. We suspect the failure of the PGSL β functional in this case is attributable to the large degree of vacuum (similar behavior was observed for the Luo-Karasiev-Trickey (LKT) functional [55] and the revised PGSL functional [50]), which could likely be ameliorated by a regularization procedure, but we did not pursue this in depth.

IV. RESULTS FOR ATOMS, DIMERS, AND NANOPARTICLES

We first establish the quality of the DPFT densities $n_3^{T \geq 0}$ and $n_{\text{Al}}^{T > 0}$ for single atoms and dimers by benchmarking against KS-DFT, OF-DFT, and coupled-cluster results. We calculate the valence densities and the all-electron densities as declared in Sec. III; all results shown are for the valence density and are obtained with PBE, unless explicitly stated otherwise; all-electron densities are labeled by “ $\mathcal{A}\mathcal{E}$ ” throughout this work; the employed numerical integration grids are declared in Table IV in Appendix B. All DPFT results reported in this work are obtained self-consistently through Eqs. (5)–(7), with the expression for the density on the right-hand side of Eq. (5) approximated by the semiclassical formulas in Eqs. (11), (12), (14), (15), and (20), respectively.

A. Single atoms

First, we consider the hydrogen atom that hosts a single electron, for which the explicit noninteracting kinetic energy functional in Eq. (9) is exact. We can therefore unambiguously benchmark the approximate semiclassical DPFT densities in Eqs. (12), (15), and (20), while illustrating some of their characteristics, albeit for $N = 1$. In Fig. 1 we find a markedly improved density tail of n_3 compared with n_{TF} , deep into

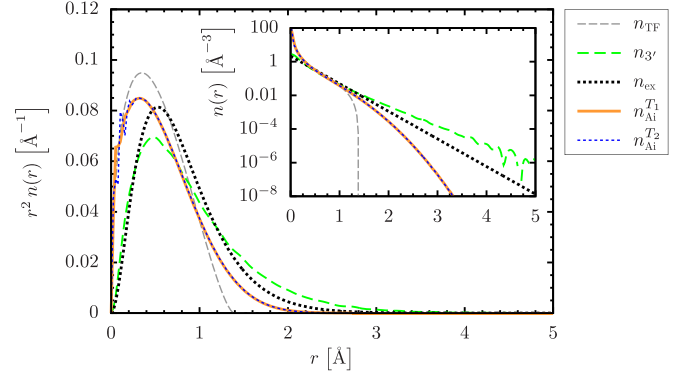


FIG. 1. Comparison of DPFT electron densities with the exact density n_{ex} of the hydrogen atom (main plot, rescaled abscissa). We show the quasiclassical TF density and its quantum-corrected successors, the semiclassical densities n_3 , as well as n_{Al}^T , at $k_{\text{B}}T_1 = 0.1 \text{ eV}$ and $k_{\text{B}}T_2 = 10^{-6} \text{ eV}$, respectively. The semiclassical densities reach deep into the classically forbidden region, where n_3 approximates the characteristic exponential decay (inset)

the classically forbidden region of the Coulomb potential, for which we employ Eq. (28). There is no difference (to the eye) when using the pseudopotential $\mathcal{C}^{(1)}$ of Eq. (29) instead. Deviations from the pure exponential decay of the exact density n_{ex} are expected since the semiclassical approximation n_3 generally performs better for larger N . The same holds for n_{Al}^T , where we find $k_{\text{B}}T_1 = 0.1 \text{ eV}$ sufficiently small for targeting the ground-state density, as we judge from comparing with the density at $k_{\text{B}}T_2 = 10^{-6} \text{ eV}$. Meaningful quality tests of n_3 , especially against KS-DFT and OF-DFT calculations, are discussed below with the aid of many-electron systems. As a general strategy for selecting low enough temperatures that yield density profiles close to the ground-state density, we start with high temperatures that incur small computational cost and decrease T until the change in density is negligible; for different systems this happens at different temperatures. As expected, the scaling behavior of n_{Al}^T near the singularity of the Coulomb potential is similar to that of n_{TF} .

While any semiclassical method can be expected to fail for $N = 1$ particle, we find in Fig. 2 that n_3 and n_3^T capture the ($N = 3$)-electron valence density of an aluminum atom adequately, especially in the regions of the atom that are important for determining bond properties. Both the KS densities with (i) LSDA and (ii) PBE exchange-correlation functional are reasonably close to the quasiclassical result from a coupled-cluster calculation [CCSD(T)]. The discontinuous derivative of n_{TF} makes convergence of the self-consistent DPFT loop troublesome when using PBE (and we thus employ n_{TF} with LDA), but converging n_3 with PBE is unproblematic. A temperature T corresponding to $k_{\text{B}}T = 0.1 \text{ eV}$ brings n_3^T close enough to its ground-state version n_3 . We find n_3 to (i) give an approximate average account of the quantum oscillations near the nucleus and (ii) approach the quality of the KS(LSDA) results in the valence region, with n_3 being superior to the KS density in some parts of the evanescent region and inferior in others. This is no small feat when bearing in mind that n_3 is only the first step in a hierarchy of systematic improvements upon the TF approximation. The quality of n_3 is further sub-

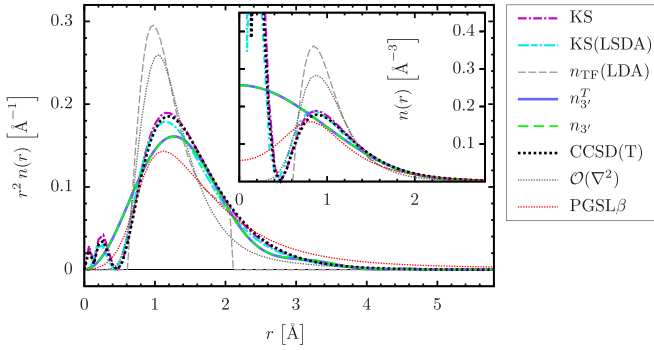


FIG. 2. DPFT electron densities like in Fig. 1, but for the valence electrons of aluminum (main plot, rescaled abscissa). We also compare the DPFT densities with those from the second-order gradient expansion $[O(\nabla^2)]$ (see, for example, Ref. [53]) and with those obtained from using the Pauli-Gaussian functional (PGSL β) from Ref. [56]. The larger deviations of n_{3^T} near the nucleus (inset) can generally be considered benign when calculating electronic properties of atomic matter, for which the valence region is key.

stantiated by the comparison with two OF-DFT approaches: In contrast to n_{3^T} , both the second-order gradient expansion $[O(\nabla^2)]$ and the Pauli-Gaussian functional (PGSL β) deviate markedly from the KS predictions in the valence region and further toward vacuum.

Figure 3 illustrates valence densities as well as all-electron densities of a magnesium atom. Both of our semiclassical approaches capture the quasixact CCSD(T) all-electron density over about eight orders of magnitude, and in particular the exponential decay in the valence region, where the valence density n_{Ai}^T follows its all-electron version and aligns with both the all-electron density $n_{3^T}(\mathcal{E})$ and the valence density

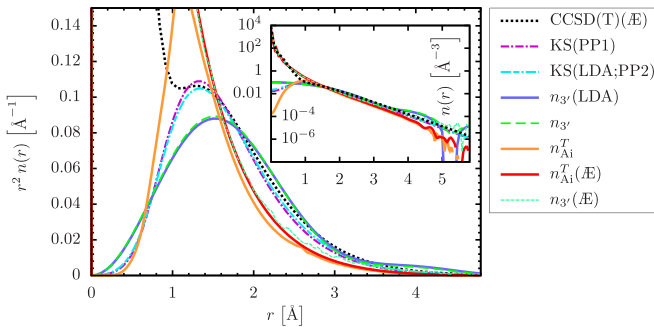


FIG. 3. DPFT electron densities like in Fig. 2, but for magnesium (main plot, rescaled abscissa). The quasixact density in the bonding region is reasonably well matched over several orders of magnitude (inset). The KS calculations are rather insensitive to different pseudopotentials: “PP1” labels the density obtained from the GGA pseudopotential of Ref. [108] (deployed together with PBE) and closely aligns with the result that stems from an alternative pseudopotential (labeled “PP2,” deployed together with LDA) from Ref. [109]. We used $k_B T = 0.05$ eV for both the valence density n_{Ai}^T and the all-electron density $n_{\text{Ai}}^T(\mathcal{E})$. In the valence region, these Airy-averaged DPFT densities align reasonably well with the OF-DFT second-order gradient expansion $[O(\nabla^2)]$, and this includes the tail into vacuum, which is overestimated by the OF-DFT Pauli-Gaussian functional (PGSL β).

from the second-order gradient expansion $[O(\nabla^2)]$. In the tail, both n_{3^T} and $n_{3^T}(\mathcal{E})$ oscillate closely around the KS and CCSD(T) densities, similar to what we observe for aluminum in Fig. 2, but in contrast to the PGSL β -based OF-DFT prediction. We observe similar profiles for n_{3^T} with LDA and PBE, respectively, except deep in the classically forbidden region, where n_{3^T} can become negative, such that its derivatives make the use of PBE unreliable. In summary, then, various reasonable settings (LDA, PBE, different pseudopotentials, valence- or all-electron density, box sizes, and resolution) all produce a similar and coherent picture for single atoms, which invites us to move on to dimers.

B. Dimers

Next, we benchmark dimer densities that include the effects of bonding. We begin with the ground-state valence density of a magnesium dimer with nuclei separated by the approximate equilibrium distance. This case reveals several properties of our semiclassical density formulas, which, for $N = 4$, do not yet operate in a truly semiclassical regime. Significant differences to the KS density can therefore be expected. Indeed, $n_{3^T}^T$ conjures up maxima at the nuclei instead of minima, consistent with what we report for a single Al atom in the inset of Fig. 2. This is usually unproblematic since the valence region is of primary interest in most applications. Furthermore, like for single atoms, the density tails of $n_{3^T}^T$ closely align with the KS predictions. To a lesser extent this also holds for n_{Ai}^T , which, on the other hand, proves superior to n_{3^T} in capturing the global pattern of the density distribution, heralded by the TF density, which is the leading term of the gradient corrected n_{Ai}^T . The stark differences between $n_{3^T}^T$ and n_{Ai}^T highlight the dissimilarity of their semiclassical origins. Indeed, since n_{Ai}^T is a particular gradient expansion whose generic level of accuracy is comparable with that of the standard second-order gradient expansion, it comes as no surprise that both methods paint a similar picture. Our second OF-DFT benchmark (PGSL β) performs well in the interior regions of the dimer and near the nuclei in particular, but less so toward vacuum, where n_{3^T} proves superior.

The valence-density profile from $n_{3^T}^T$ for the Al dimer in Fig. 5 (inset) follows a pattern similar to that of the Mg dimer in Fig. 4, but better performance can be expected from our semiclassical densities for larger particle numbers. Indeed, as we show in Fig. 5 (main plot), it is reassuring that the semiclassical expression n_{Ai}^T delivers a reasonable approximation of the KS density of all 26 electrons of the Al dimer across more than eight orders of magnitude.

C. Aluminum nanoparticle

Finally, we benchmark n_{Ai}^T and $n_{3^T}^T$ against KS densities of a Wulff-shaped nanoparticle composed of 201 aluminum atoms, whose nearest-neighbor distance is fixed to the approximate bulk equilibrium separation of 2.86 Å of the fcc structure. The particle is shown in Fig. 6. Figures 6 and 7 show the valence densities of the nanoparticle, analogous to the dimer densities in Fig. 4 and the inset of Fig. 5. Overall, the patterns of the DPFT densities are what we naively expect based on the dimer simulations in Sec. IV B: $n_{3^T}^T$ captures the bonding (valence)

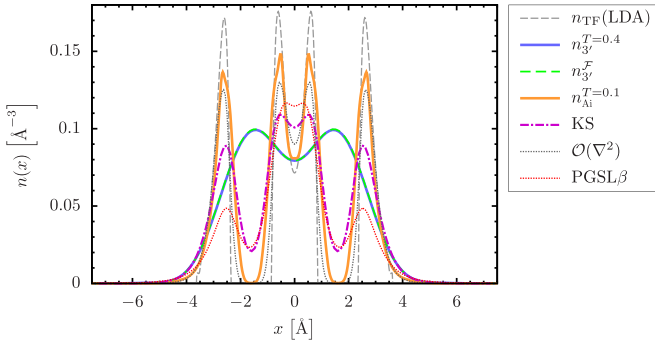


FIG. 4. The valence densities from DPFT, KS-DFT, and OF-DFT [$\mathcal{O}(\nabla^2)$ and PGSL β] calculations along the nuclear axis of a magnesium dimer with nuclei positioned at $x \approx \pm 1.60$ Å, i.e., separated by the approximate equilibrium distance of 3.21 Å. We show the densities n_3^T for a temperature $T = 0.4$ eV/ k_B , low enough for matching n_3^F almost exactly, and n_{Ai}^T for $k_B T = 0.1$ eV. For anisotropic high-resolution setups like our Mg-dimer simulation here, n_3^T is computationally more efficient than n_3 , and n_3^F . Figure 11 in Appendix B displays contour plots of n_3^T and n_{Ai}^T for the Mg dimer.

regions and the region near the surface of the nanoparticle, but exhibits unphysical oscillations into negative densities in the far tails and fails to decrease toward the nuclei. In line with our results for the Mg dimer, n_{Ai}^T predicts the overall density of the nanoparticle more accurately, especially deep into the evanescent region, where n_{Ai}^T outperforms the standard second-order gradient expansion, but overestimates the amplitudes of the density modulations in the bulk. Interestingly, when comparing the bond regions in Figs. 5 and 6, we find n_3^T to perform much better for the nanoparticle than for the Al dimer. The improved behavior of n_3^T stems from its nonlocality, where information is drawn from an extended region around the focal point \mathbf{r} . Given up to six nearest-neighbor atoms (i.e., 21 valence electrons) in the vicinity of each bond region of the nanoparticle, it is then not surprising that the averaging effect of n_3^T improves the electron densities relative to the

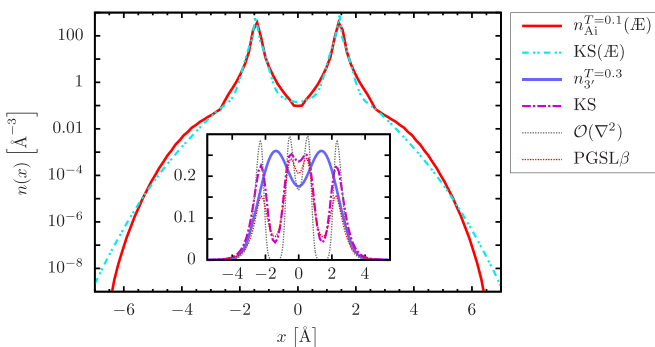


FIG. 5. All-electron densities (main plot) and valence densities (inset) of the aluminum dimer with nuclei separated by the approximate equilibrium distance of 2.86 Å. The behavior of the DPFT valence density (n_3^T for $k_B T = 0.3$ eV) relative to the densities from KS-DFT and OF-DFT [$\mathcal{O}(\nabla^2)$ and PGSL β] is consistent with our findings for the magnesium dimer in Fig. 4. The all-electron DPFT density $n_{\text{Ai}}^T(\mathcal{E})$ for $k_B T = 0.1$ eV aligns well with the KS prediction.

bond region of the aluminum dimer, where only six valence electrons contribute.

The Airy-averaged expression n_{Ai}^T , on the other hand, performs very well exactly where it is designed to do so, namely in the evanescent region across the boundary of classically allowed and forbidden regions. This is evident on the logarithmic scales of Figs. 7 and 8, where we compare KS results with the Airy-averaged valence density and its all-electron version, respectively. Given the variability of KS calculations across different settings, like LDA vs PBE and valence vs all-electron calculations, as exemplified in Figs. 7 and 8, we find $n_{\text{Ai}}^T(\mathcal{E})$ in Fig. 8 to match the all-electron KS density reasonably well over eight orders of magnitude, which encompass all parts of the nanoparticle: the electronic structure close to the nuclei, the bond regions, and the exponential decay of the density into vacuum.

V. CONCLUSIONS AND PERSPECTIVES

In this work we extended the semiclassical machinery of density-potential-functional theory (DPFT) from low-dimensional settings to three dimensions. Specifically, we developed semiclassical expressions for particle densities and energies of isolated systems that scale (quasi)linearly with particle number and thus enable, for example, electronic structure calculations of mesoscopic molecules and nanoparticles. Most importantly, those expressions, which we derived in complete analogy to their low-dimensional versions and without relying on *ad hoc* measures or assumptions, are void of free parameters and can be further improved in a systematic manner. These characteristics put the semiclassical DPFT formalism that has been developed over the last decade in stark contrast to many contemporary approaches to density functional theory in general and to its orbital-free variants in particular.

To illustrate the generic semiclassical features as well as the practical aspects of our DPFT implementation, we put an emphasis on the calculation of particle densities, also because the improvements of the semiclassical energies upon the Thomas-Fermi model are less convincing, at least for the cases studied here. DPFT was used to simulate real-world composite atomic systems, specifically, the electronic structure of metal dimers and nanoparticles. As expected, the semiclassical DPFT densities become more accurate as the particle number increases. Indeed, for the 603 (2613) electrons of the valence (all-electron) density of a nanoparticle composed of 201 aluminum atoms, their quality is competitive with that of generic Kohn-Sham calculations.

Our two particle-density expressions n_{Ai} and n_3 deliver accurate results in different regimes and for different reasons. The semilocal Airy averaged n_{Ai} is exact for linear (effective) potentials and is therefore particularly accurate in the evanescent tails toward vacuum. While we may speculate that further systematic improvements are attainable by making a successor of n_{Ai} exact also for quadratic or higher-order polynomials, this route is unexplored at present. In contrast, the common feature of $n_3(\mathbf{r})$ and its successors is their reliance on the (effective) potential in an extended region around the focal position \mathbf{r} , which makes them particularly powerful in the bulk. The split-operator based n_3 represents the first step

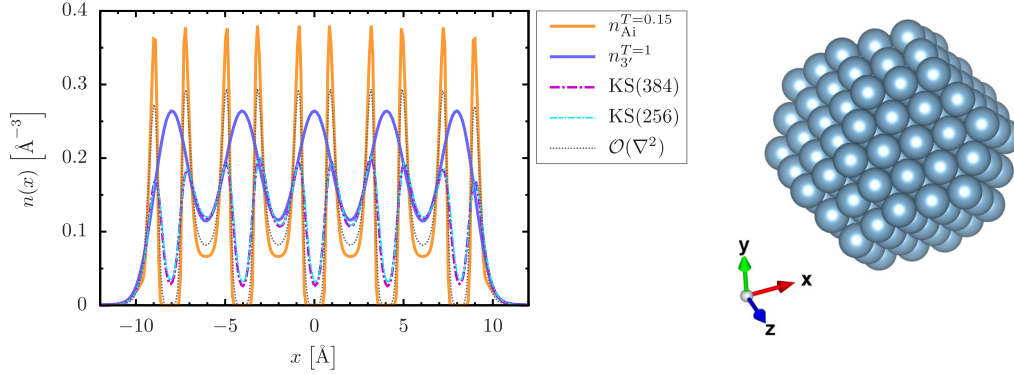


FIG. 6. Cut through the valence densities along the x axis (left) of a Wulff-shaped 201-Al-atom nanoparticle (right), as predicted by the semiclassical DPFT formulas n_{Ai}^T and $n_{3'}^T$. The KS densities were computed on grids of 256^3 and 384^3 points, respectively. The discrepancies between $n_{3'}^T$ and the KS densities in the bond region are less pronounced if electrons of several atoms contribute to the electron density between any two nuclei, rather than only two atoms like for the dimers in Figs. 4 and 5. The Airy-averaged DPFT density overestimates the density variations in the bulk more than the second-order gradient expansion [$O(\nabla^2)$] does.

in a ladder of explicit systematic approximations, and two more rungs have already been derived and benchmarked. In fact, the most accurate of these expressions has the same computational complexity as $n_{3'}$, with the proviso that the special function at its heart can eventually be computed efficiently, just like the underlying Bessel function at the core of $n_{3'}$. Also, the inaccurate semiclassical energies that are associated with the two approximation schemes employed here are bound to improve once suitable implementations of the higher-order corrections are available.

The increase in accuracy through higher-order DPFT approximations will generally decrease computational efficiency, and problem-specific tradeoffs between accuracy and efficiency will have to be made in future applications of semiclassical DPFT. Transferability, however, does not need to be sacrificed along this route. The systematic nature of the here developed functional approximations makes them universally applicable across external potentials and types of interactions.

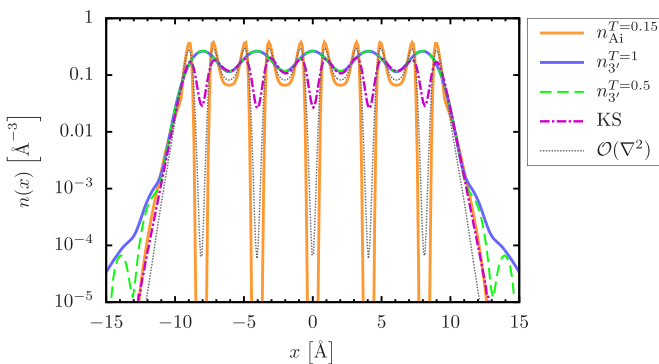


FIG. 7. The valence densities of $n_{\text{Ai}}^{T=0.15}$ and $n_{3'}^{T=1}$ like in Fig. 6, but on a logarithmic scale. Only the transitional region toward vacuum exhibits significant deviations between $n_{3'}^T$ at $k_B T = 1$ eV and $n_{3'}^{T=0.5}$, respectively. There, $n_{3'}$ generally becomes unreliable anyway, while the performance of $n_{\text{Ai}}^{T=0.15}$ incidentally leaves nothing to be desired and outperforms the OF-DFT result from the standard second-order gradient expansion [$O(\nabla^2)$].

ACKNOWLEDGMENTS

We are grateful to B.-G. Englert for most valuable input and insights. This work has been supported by the National Research Foundation, Singapore, and A*STAR under its CQT Bridging Grant and its Quantum Engineering Programme. S.M. acknowledges the support provided by BC DRI Group and the Digital Research Alliance of Canada.

APPENDIX A: DERIVATION OF DPFT ENERGIES AND DENSITIES IN 3D

In this Appendix we derive the semiclassical potential functionals for the finite-temperature single-particle densities presented in Eqs. (14), (15), and (20), together with the associated kinetic energies.

1. Suzuki-Trotter-approximated densities and energies

Derivation of $n_{3'}^T$. We start with deriving Eq. (15) from the finite-temperature version

$$n^T(\mathbf{r}) = g(\mathbf{r}|\eta_T(\mu - H)|\mathbf{r}) \quad (\text{A1})$$

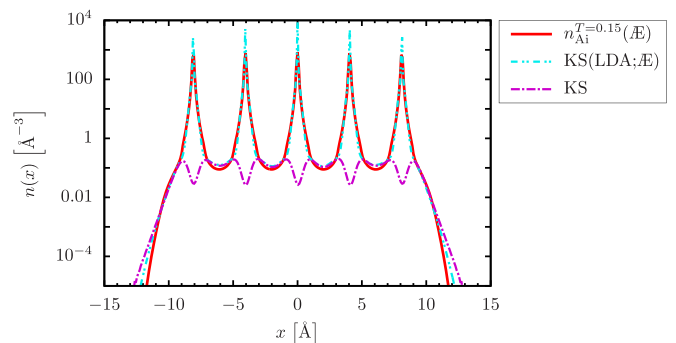


FIG. 8. Comparison of the all-electron density $n_{\text{Ai}}^{T=0.15}(\mathcal{E})$ with the all-electron KS density (LDA) along the x axis; see Fig. 11 in Appendix B for $n_{\text{Ai}}^{T=0.15}(\mathcal{E})$ in the $z = 0$ plane. The KS valence density (PBE) is the same as that shown in Figs. 6 and 7.

of Eq. (10). Upon approximating the time-evolution operator by $U_{3'}$ and inverting the Fourier transform of $\eta_T(\dots)$ in Eq. (10), we arrive at

$$n_{3'}^T(\mathbf{r}) = g \int \frac{(\mathbf{dp}_1)(\mathbf{dp}_2)(\mathbf{dr}_1)}{(2\pi\hbar)^{2D}} \exp\left(\frac{i}{\hbar}\mathbf{r}_1 \cdot (\mathbf{p}_1 - \mathbf{p}_2)\right) \times \eta_T(\mu - H_{3'}), \quad (\text{A2})$$

where $H_{3'} = (\mathbf{p}_1^2 + \mathbf{p}_2^2)/(4m) + V(\mathbf{r} + \mathbf{r}_1)$. With $\mathbf{p} = \hbar\mathbf{k}$ we write

$$\begin{aligned} n_{3'}^T(\mathbf{k}) &= \mathcal{F}\{n_{3'}^T(\mathbf{r}')\}(\mathbf{k}) = \int (\mathbf{dr}') e^{-i\mathbf{kr}'} n_{3'}^T(\mathbf{r}') \\ &= \frac{g}{(2\pi)^{2D}} \int (\mathbf{dk}_1)(\mathbf{dk}_2)(\mathbf{dr}_1) e^{i\mathbf{r}_1 \cdot (\mathbf{k}_1 - \mathbf{k}_2)} \end{aligned}$$

$$\begin{aligned} n_{3'}^T(\mathbf{k}) &= \frac{g}{(2\pi)^D} \int (\mathbf{dk}_1)(\mathbf{dk}_2) \int \frac{(\mathbf{dr}_1)}{(2\pi)^D} \underbrace{e^{i\mathbf{r}_1 \cdot (\mathbf{k} + \mathbf{k}_1 - \mathbf{k}_2)}}_{\delta(\mathbf{k} + \mathbf{k}_1 - \mathbf{k}_2)} \int (\mathbf{dr}') e^{-i\mathbf{kr}'} \eta_T\left(\mu - \frac{\mathbf{k}_1^2 + \mathbf{k}_2^2}{4m/\hbar^2} - V(\mathbf{r}')\right) \\ &= \frac{g\Omega_D}{(2\pi)^D} \int (\mathbf{dr}') e^{-i\mathbf{kr}'} \int_0^\infty dk_1 k_1^{D-1} \eta_T\left(\mu - V(\mathbf{r}') - \frac{\hbar^2\mathbf{k}^2}{8m} - \frac{\hbar^2\mathbf{k}_1^2}{2m}\right) \end{aligned} \quad (\text{A3})$$

identifies the Fourier transform of the polylogarithm $\text{Li}_{D/2}$ of order $D/2$ after evaluation of the k_1 integral:

$$n_{3'}^T(\mathbf{k}) = -g \left(\frac{m k_B T}{2\pi\hbar^2}\right)^{D/2} \int (\mathbf{dr}') e^{-i\mathbf{kr}'} \text{Li}_{D/2}(z). \quad (\text{A6})$$

Here, $z = -tb$, $t(\mathbf{r}') = e^\sigma$, $\sigma(\mathbf{r}') = [\mu - V(\mathbf{r}')]/(k_B T)$, and $b(k) = \exp[-\hbar^2 k^2/(8m k_B T)]$. Since $D/2 > 0$ and $z < 0$, we may use the integral representation

$$\begin{aligned} \text{Li}_{D/2}(z) &= - \int_0^\infty dx \frac{tbc}{d + tb} \\ &= - \int_0^\infty dx \int_0^\infty dy t(\mathbf{r}') e^{-y\sigma(\mathbf{r}')} c e^{-yd/b(k)}, \quad (\text{A7}) \end{aligned}$$

with $c = x^{D/2-1}/\Gamma[D/2]$ and $d = e^x$, thereby disentangling the \mathbf{r}' dependence of $\text{Li}_{D/2}(z)$ from its k dependence, which allows us to obtain Eq. (15) from the inverse Fourier transform of

$$\begin{aligned} n_{3'}^T(\mathbf{k}) &= \frac{g}{\Gamma[D/2]} \left(\frac{k_B T}{2\pi\hbar^2}\right)^{D/2} \int_0^\infty dy \\ &\times \int (\mathbf{dr}') e^{-i\mathbf{kr}'} \underbrace{e^{\sigma - y \exp(\sigma)}}_{f_y(\mathbf{r}')} \underbrace{\int_0^\infty dx x^{D/2-1} e^{-y \exp(x+\kappa)}}_{g_y^D(k)}. \end{aligned} \quad (\text{A8})$$

Both f_y and g_y^D [cf. Eqs. (16) and (17)] are sufficiently suppressed for $y \gtrsim 40$. We may thus restrict the support of the y integral to $0 < y < 40$ and calculate it with an adaptive quadrature: we use the Boole rule. For each value of y the inverse fast Fourier transform in Eq. (15) delivers all values on the spatial grid of size G in one go, resulting in a computational cost of $n_{3'}^T(\mathbf{r})$ that scales like $G \ln G$. This contrasts with Eq. (12), where the density $n_{3'}(\mathbf{r})$ at each of the G grid points, indexed by \mathbf{r} , requires a summation over

$$\times \int (\mathbf{dr}') e^{-i\mathbf{kr}'} \eta_T\left(\mu - \frac{\mathbf{k}_1^2 + \mathbf{k}_2^2}{4m/\hbar^2} - V(\mathbf{r}' + \mathbf{r}_1)\right) \quad (\text{A3})$$

for the Fourier transform of $n_{3'}^T(\mathbf{r})$, where we denote the Fourier transform of a function $f(\mathbf{r})$ as $f(\mathbf{k}) = \mathcal{F}\{f(\mathbf{r})\}(\mathbf{k}) = \int (\mathbf{dr}) e^{-i\mathbf{kr}} f(\mathbf{r})$ and implement \mathcal{F} as a fast Fourier transform using the FFTW library for C++ [110]. Defining $\mathbf{r}_2 = \mathbf{r}' + \mathbf{r}_1$, we express the last integral in Eq. (A3) as

$$e^{i\mathbf{kr}_1} \int (\mathbf{dr}_2) e^{-i\mathbf{kr}_2} \eta_T\left(\mu - \frac{\mathbf{k}_1^2 + \mathbf{k}_2^2}{4m/\hbar^2} - V(\mathbf{r}_2)\right), \quad (\text{A4})$$

such that

the whole grid. Naturally, there is a tradeoff between grid size and accurate enough evaluation of the y integral, as a rule of thumb, $n_{3'}^T$ outperforms $n_{3'}$ for $G \gtrsim 50^3$ and $n_{3'}^F$ (see below) for $G \gtrsim 100^3$.

Since g_y^D diverges for $y \rightarrow 0$, we calculate the y integral from 0 to $\epsilon \ll 1$ separately from the rest of $n_{3'}^T(\mathbf{r})$. For $y \ll 1$, we have $f_y(\mathbf{r}') \approx e^\sigma (1 - y e^\sigma)$, such that

$$\begin{aligned} &\int_0^\epsilon dy \mathcal{F}\{f_y(\mathbf{r}')\}(\mathbf{k}) g_y^D(k) \\ &\approx \mathcal{F}\{e^{\sigma(\mathbf{r}')}\}(\mathbf{k}) \\ &\times \int_0^\epsilon dy g_y^D(k) - \mathcal{F}\{e^{2\sigma(\mathbf{r}')}\}(\mathbf{k}) \int_0^\epsilon dy y g_y^D(k). \end{aligned} \quad (\text{A9})$$

Both $\int_0^\epsilon dy g_y^D(k)$ and $\int_0^\epsilon dy y g_y^D(k)$ are bounded from above by $e^{-\kappa}\Gamma(D/2)$ (for any $\epsilon > 0$), and the auxiliary functions $g_y^D(k)$ can be evaluated numerically, tabulated, and interpolated. Starting with any initial guess for ϵ , adequately small values of ϵ are identified during the adaptive y integration. Alternatively, we may replace the lower integration limit in Eq. (A8) by a small value like $y = 10^{-300}$.

Derivation of $n_{3'}^F$. For anisotropic situations at $T = 0$, it is expedient to rephrase the density $n_{3'}$ of Eq. (12) in terms of fast Fourier transforms, as done in [38]. The resulting $n_{3'}^F$ still scales like G^2 , but the computational cost is reduced by a factor of ~ 10 – 40 since only exponentials (not Bessel functions) have to be evaluated: Retracing Eqs. (A1)–(A5) with $\eta_{T \rightarrow 0}(\cdot) = \eta(\cdot)$, we get

$$\begin{aligned} n_{3'}(\mathbf{k}) &= \frac{g\Omega_D}{(2\pi)^D} \int (\mathbf{dr}') e^{-i\mathbf{kr}'} \int_0^\infty dk_1 k_1^{D-1} \eta(Q^2 - \hbar^2\mathbf{k}_1^2) \\ &= \frac{g\Omega_D}{(2\pi)^D} \int (\mathbf{dr}') e^{-i\mathbf{kr}'} \frac{Q^D}{D} \eta(Q^2), \end{aligned} \quad (\text{A10})$$

where $Q^2 = 2m[\mu - V(\mathbf{r}')] - \frac{\hbar^2\mathbf{k}^2}{4}$, which results in Eq. (14).

Kinetic energy. We obtain approximations of the (ground-state) kinetic energy

$$E_{\text{kin}} = -\frac{\hbar^2}{2m} \int (\text{d}\mathbf{r}) (\nabla_{\mathbf{r}}^2 n^{(1)}(\mathbf{r}; \mathbf{r}'))_{\mathbf{r}'=\mathbf{r}} \quad (\text{A11})$$

in terms of the effective potential V by deriving approximate one-body reduced density matrices $n^{(1)}(\mathbf{r}; \mathbf{r}')$. With the Hamiltonian $H = T + V$, Eq. (3) becomes

$$E_{\text{kin}} = E_1[V - \mu] - \int (\text{d}\mathbf{r}) [V(\mathbf{r}) - \mu] n(\mathbf{r})$$

$$n_{3'}^{(1)}(\mathbf{r}; \mathbf{r}') = g \int \frac{\text{d}t}{2\pi i t} e^{\frac{i}{\hbar} \mu t} \langle \mathbf{r} | U_{3'}(t) | \mathbf{r}' \rangle = g \int (\text{d}\mathbf{a}) \left(\frac{k_{3'}}{2\pi b} \right)^D J_D(2b k_{3'}), \quad (\text{A13})$$

which is consistent with the Suzuki-Trotter approximation inherent to $n_{3'}$. Equation (A13) follows the structure of Eq. (12) with $b = \sqrt{a^2 + (\mathbf{a} + \mathbf{r} - \mathbf{r}')^2}$ and yields Eq. (13):

$$E_{\text{kin}}^{(3')} = -\frac{\hbar^2}{2m} \int (\text{d}\mathbf{r}) [\nabla_{\mathbf{r}}^2 n_{3'}^{(1)}(\mathbf{r}; \mathbf{r}')]_{\mathbf{r}'=\mathbf{r}} = \frac{g \Omega_D}{(2\pi \hbar)^D (2D+4)m} \int (\text{d}\mathbf{r}) \{2m[\mu - V(\mathbf{r})]\}_+^{\frac{D+2}{2}}, \quad (\text{A14})$$

which can be calculated in lieu of the finite-temperature kinetic energy $E_{\text{kin}}^{(3'),T}$ for small enough T .

2. Airy-averaged density and energy

With the help of Eq. (19) and defining $F(A = H - \mu) = \mathcal{E}_T(H - \mu)$ [cf. Eq. (9)], with derivative $F'(A) = \frac{\partial F(A)}{\partial V} = f(A) = \eta_T(H - \mu)$, we write the functional $E_1[V - \mu]$ from Eq. (8) and its functional derivative as

$$\begin{aligned} E_1[V - \mu] &= \text{tr}\{F(A)\} = g \int \frac{(\text{d}\mathbf{r})(\text{d}\mathbf{p})}{(2\pi \hbar)^3} [F(A)]_{\text{W}} \\ &\cong E_1^{\text{Ai},T}[V - \mu] = \frac{g}{(2\pi \hbar)^3} \int (\text{d}\mathbf{r}) \int (\text{d}\mathbf{p}) \left\langle F(\tilde{A}_{\text{W}}) - \frac{\hbar^2(\nabla^2 V)}{12m} F''(\tilde{A}_{\text{W}}) \right\rangle_{\text{Ai}} \end{aligned} \quad (\text{A15})$$

and

$$\begin{aligned} n[V - \mu] &= g \int \frac{(\text{d}\mathbf{p})}{(2\pi \hbar)^3} [f(A)]_{\text{W}} \\ &\cong n_{\text{Ai}}^T[V - \mu] = \frac{g}{(2\pi \hbar)^3} \int (\text{d}\mathbf{p}) \left\langle f(\tilde{A}_{\text{W}}) - \frac{\hbar^2(\nabla^2 V)}{12m} f''(\tilde{A}_{\text{W}}) \right\rangle_{\text{Ai}}, \end{aligned} \quad (\text{A16})$$

respectively. With

$$\int_0^\infty \text{d}p 4\pi p^2 f(\tilde{A}_{\text{W}}) = -(2\pi m k_{\text{B}} T)^{3/2} \text{Li}_{3/2}(-e^{-v_x(\mathbf{r})}) \quad (\text{A17})$$

and, in cylindrical coordinates $\{q = \sqrt{p_x^2 + p_y^2}, \phi, p_z\}$,

$$\begin{aligned} \int (\text{d}\mathbf{p}) f''(\tilde{A}_{\text{W}}) &= \int \text{d}p_z \frac{2\pi}{(k_{\text{B}} T)^2} \int_0^\infty \text{d}q q f''(\tilde{A}_{\text{W}}) \\ &= \frac{2}{(k_{\text{B}} T)^2} \int_0^\infty \text{d}p_z \frac{2\pi m k_{\text{B}} T}{4 \cosh^2[v_x/2 + p_z^2/(4m k_{\text{B}} T)]} \\ &= -\frac{(2\pi m k_{\text{B}} T)^{3/2}}{(k_{\text{B}} T)^2} \text{Li}_{-1/2}(-e^{-v_x(\mathbf{r})}), \end{aligned} \quad (\text{A18})$$

we get

$$n_{\text{Ai}}^T[V - \mu] = -g \frac{(2\pi m k_B T)^{3/2}}{(2\pi \hbar)^3} \int dx \text{Ai}(x) \left\{ \text{Li}_{3/2}(-e^{-v_x(\mathbf{r})}) - \frac{\hbar^2(\nabla^2 V)}{12m(k_B T)^2} \text{Li}_{-1/2}(-e^{-v_x(\mathbf{r})}) \right\} \quad (\text{A19})$$

and, with $\frac{\partial}{\partial V} \text{Li}_s(-e^{-v_x(\mathbf{r})}) = -\frac{1}{k_B T} \text{Li}_{s-1}(-e^{-v_x(\mathbf{r})})$,

$$E_1^{\text{Ai},T}[V - \mu] = \frac{-g(m k_B T)^{3/2}}{(2\pi)^{3/2} \hbar^3} \int (d\mathbf{r}) \int dx \text{Ai}(x) \left\{ -(k_B T) \text{Li}_{5/2}(-e^{-v_x(\mathbf{r})}) + \frac{\hbar^2(\nabla^2 V)}{12m(k_B T)} \text{Li}_{1/2}(-e^{-v_x(\mathbf{r})}) \right\}. \quad (\text{A20})$$

The TF density at finite temperature, which reads

$$n_{\text{TF}}^T[V - \mu] = -g \left(\frac{m}{2\pi \hbar^2} \right)^{D/2} (k_B T)^{D/2} \text{Li}_{D/2}(-e^{-v(\mathbf{r})}) \quad (\text{A21})$$

in D dimensions, is recovered from Eq. (A19) in the case of constant V . Analogously,

$$E_1^{\text{TF},T}[V - \mu] = g \left(\frac{m}{2\pi \hbar^2} \right)^{D/2} (k_B T)^{\frac{D+2}{2}} \text{Li}_{\frac{D+2}{2}}(-e^{-v(\mathbf{r})}). \quad (\text{A22})$$

We find Eq. (20) from integrating Eq. (A19) by parts and exhibiting the units of energy (\mathcal{E}) and length (\mathcal{L}). Analogously, we reveal the computationally more feasible expression

$$E_1^{\text{Ai},T}[V - \mu] = -u_0 \times \begin{cases} a(\mathbf{r}) \int (d\mathbf{r}') \int dx \mathcal{A}(x) [u_1 \text{Li}_{3/2}(-e^{-v_x(\mathbf{r})}) + u_2(\mathbf{r}) \text{Li}_{-1/2}(-e^{-v_x(\mathbf{r})})], & a(\mathbf{r}) > 0 \\ (k_B T) \int (d\mathbf{r}') [u_1 \text{Li}_{3/2}(-e^{-v_0(\mathbf{r})}) + u_2(\mathbf{r}) \text{Li}_{-1/2}(-e^{-v_0(\mathbf{r})})], & a(\mathbf{r}) = 0 \end{cases} \quad (\text{A23})$$

for Eq. (A20) [see Eqs. (21)–(24)].

APPENDIX B: ADDITIONAL DETAILS ON THE NUMERICS AND MISCELLANEOUS RESULTS

In this Appendix, we spell out expedient procedures for the numerical evaluation of the DPFT densities and energies. We also analyze the semiclassical density and energy formulas applied to harmonically confined fermion gases and to the dissociation of hydrogen.

1. Hartree potential

We implement the Hartree potential as follows: With the Fourier transform $n(\mathbf{k})$ of the spatial density $n(\mathbf{r})$, we write the Hartree energy as

$$E_{\text{H}}[n] = \frac{W}{2} \int (d\mathbf{r})(d\mathbf{r}') \frac{n(\mathbf{r})n(\mathbf{r}')}{|\mathbf{r} - \mathbf{r}'|} = \frac{W}{2} \int \frac{(d\mathbf{k})}{(2\pi)^3} 4\pi \frac{n(\mathbf{k})n(-\mathbf{k})}{k^2}, \quad (\text{B1})$$

TABLE I. An equidistantly spaced integration grid demands a high resolution for extracting high-precision energies. The exact kinetic energy of hydrogen equals the binding energy of $E_{\text{B}} = 13.6057$ eV, and can be obtained from the virial theorem since we can evaluate the energy functionals with the known exact density: $E_{\text{kin}}^{\text{vir}}[n_{\text{ex}}] = -E_{\text{ext}}[n_{\text{ex}}]/2$. For comparison we report the kinetic energies based on both the exact Coulomb potential and the all-electron pseudopotential of Eq. (28). Alternatively, we may enlist the von Weizsäcker kinetic energy $E_{\text{kin}}^{\text{vW}}[n_{\text{ex}}] = 9 \times E_{\text{kin}}^{\text{v}^2}[n_{\text{ex}}]$, which is exact for single-orbital ground states, while the Thomas-Fermi kinetic energy functional $E_{\text{kin}}^{\text{TF}}[n]$ is inadequate, even when supplemented with the leading gradient correction $E_{\text{kin}}^{\text{v}^2}[n]$. All energies are given in eV.

Functional	Steps for integration grid					analytical energy
	64	128	256	384	512	
$E_{\text{kin}}^{\text{vir}}$	13.2171	13.5073	13.5810	13.5947	13.5995	13.6057
$E_{\text{kin}}^{\text{vir}}$ [Eq. (28)]	13.4886	13.5891	13.6034	13.6050	13.6054	–
$E_{\text{kin}}^{\text{vW}}$	13.0525	13.5403	13.5979	13.6034	13.6047	13.6057
$E_{\text{kin}}^{\text{TF}} + E_{\text{kin}}^{\text{v}^2}$	9.28932	9.37014	9.37831	9.37902	9.37918	9.37930

TABLE II. The self-consistent kinetic and total energies of hydrogen from the DPFT densities (cf. Fig. 1) are of no use, although the total energy $E^{\text{Ai},T} = E_{\text{kin}}^{\text{Ai},T} + E_{\text{ext}}[n_{\text{Ai}}^T]$ for $k_B T = 10^{-6}$ eV is not too far off the exact value $E_{\text{kin}}^{\text{vW}}[n_{\text{ex}}] + E_{\text{ext}}[n_{\text{ex}}] = -13.6057$ eV. All energies are given in eV.

$E_{\text{kin}}^{\text{TF}}$	E^{TF}	$E_{\text{kin}}^{3'}$	$E^{3'}$	$E_{\text{kin}}^{\text{Ai},T}$	$E^{\text{Ai},T}$
26.46	-28.06	26.49	-0.9095	40.48	-12.05

whose discretized version is ill defined due to the divergent summand at $k = 0$. We regularize this singularity by adding and subtracting $n(\mathbf{k} = 0)^2 e^{-k^2} = N^2 e^{-k^2}$ in the numerator of Eq. (B1):

$$\begin{aligned}
 E_{\text{H}}[n] &= \frac{W}{4\pi^2} \left[\lim_{k \rightarrow 0} \frac{n(\mathbf{k})n(-\mathbf{k}) - N^2 e^{-k^2}}{k^2} \right. \\
 &\quad + \Delta k^3 \left(\sum_{\mathbf{k} \neq 0} \frac{n(\mathbf{k})n(-\mathbf{k}) - N^2 e^{-k^2}}{k^2} \right) \\
 &\quad \left. + \int (d\mathbf{k}) \frac{N^2 e^{-k^2}}{k^2} \right] \\
 &= \frac{W}{4\pi^2} \left[N^2 + \Delta k^3 \left(\sum_{\mathbf{k} \neq 0} \frac{n(\mathbf{k})n(-\mathbf{k}) - N^2 e^{-k^2}}{k^2} \right) \right. \\
 &\quad \left. + 2\pi^{3/2} N^2 \right], \tag{B2}
 \end{aligned}$$

where Δk is the lattice spacing in Fourier space. For the equality in Eq. (B2) to hold, we assume that $\nabla_{\mathbf{k}}[n(\mathbf{k})n(-\mathbf{k})]$ decays faster than $2\mathbf{k}$ as $|\mathbf{k}| \rightarrow 0$. The same procedure regularizes the Hartree potential

$$\begin{aligned}
 V_{\text{H}}(\mathbf{r}) &= W \int (d\mathbf{r}') \frac{n(\mathbf{r}')}{|\mathbf{r} - \mathbf{r}'|} \\
 &= 4\pi W \left[\mathcal{F}^{-1} \left\{ \frac{n(\mathbf{k}) - N e^{-k^2}}{k^2} \Big|_{\mathbf{k} \neq 0} + N \Big|_{\mathbf{k}=0} \right\} (\mathbf{r}) \right. \\
 &\quad \left. + \frac{N}{4\pi^2} \left(\frac{\pi}{r} \text{Erf}(r/2) \Big|_{r \neq 0} + \sqrt{\pi} \Big|_{r=0} \right) \right]. \tag{B3}
 \end{aligned}$$

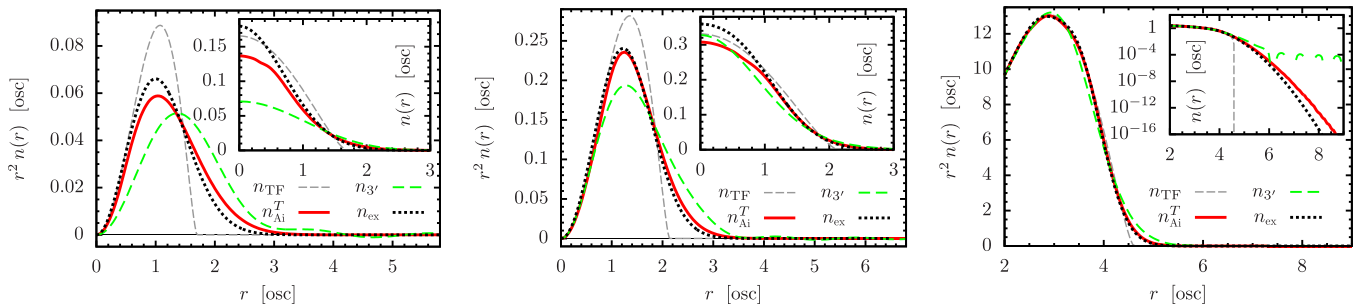


FIG. 9. Unsurprisingly, the quality of the semiclassical densities improves with larger particle number N , here illustrated with the aid of noninteracting unpolarized spin- $\frac{1}{2}$ fermions in a harmonic trap for $N = 1$ (left), $N = 4$ (center), and $N = 400$ (right). The exact densities for large particle numbers are generated with the (fractionally filled) shell densities reported in Ref. [114].

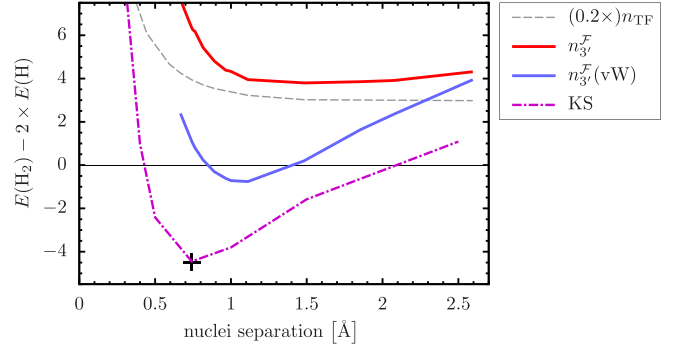


FIG. 10. $E_{\text{kin}}^{\text{vW}}$, evaluated with $n_{3'}^{\text{F}}$, yields a qualitatively correct dissociation curve when benchmarked against the self-consistent KS(PBE) energies. The self-consistent $n_{3'}^{\text{F}}$ binds the two hydrogen atoms, albeit weakly, and it is well known that the self-consistent TF density does not. We thus echo the well-known insight that an accurate kinetic energy is essential for getting the dissociation right. Eventually, however, the self-consistent DPFT energies associated with the DPFT density formulas deployed in this work are not accurate enough, given today's demands on electronic structure calculations (see also Table II).

The computational cost of both $E_{\text{H}}[n]$ and $V_{\text{H}}(\mathbf{r})$ scales like $G \ln G$.

2. Regularizations of the DPFT densities and energies

The approximate semiclassical densities do not possess all the features of the exact density. In particular, n_3 , $n_{3'}^{\text{F}}$, and $n_{3'}^{\text{T}}$ can exhibit oscillations around zero in the classically forbidden region. We therefore evaluate exchange-correlation functionals that demand non-negative densities with $[n[V]]_+$ instead of $n[V]$. This procedure is only justified if negative densities are small in magnitude, which is usually the case for large enough N and (in case of $n_{3'}^{\text{T}}$ or n_{Ai}^{T}) temperatures that are large enough while retaining the ground-state character of the density profiles. Furthermore, the PBE functional requires spatial derivatives of the densities, and both n_{Ai}^{T} and $E_{\text{kin}}^{\text{Ai},T}$ require the gradient and the Laplacian of the effective potential V . If the numerical differentiation introduces instabilities in the self-consistent DPFT loop for strong interactions and if many iterations are required, we regularize the numerical derivatives in a three-step process: The first and second partial derivatives are obtained via fast Fourier transform after

TABLE III. The self-consistent DPFT energies E for spin-unpolarized spin- $\frac{1}{2}$ fermions in a 3D harmonic trap reaffirm that the semiclassical approximations improve as the particle number increases. The exact energies are $E_{\text{ex}}(N = 4) = 8$ and $E_{\text{ex}}(N = 400) = 3210$ in harmonic oscillator units.

N	Density	Steps	E_{kin}	E_{ext}	E	Relative error (%)	Absolute error per particle ($\hbar\omega$)
4	n_{TF}	104	3.434	3.437	6.872	14	0.282
	n_{TF}	384	3.434	3.434	6.868	14	0.283
	$n_{\text{Ai}}^{T=0.1}$	104	3.742	3.761	7.503	6	0.124
	$n_{\text{Ai}}^{T=0.1}$	384	3.740	3.762	7.503	6	0.124
400	n_{TF}	104 and 384	1594	1594	3188	0.7	0.055
	$n_{3'}$	104 and 384	1594	1636	3230	0.6	0.050
	$n_{3'}^{T=1}$	104	1412	1722	3134	2.3	0.190
	$n_{3'}^{T=0.1}$	104	1586	1634	3220	0.3	0.025
	$n_{\text{Ai}}^{T=0.1}$	104	1574	1615	3189	0.7	0.053
	$n_{\text{Ai}}^{T=0.01}$	104	1573	1615	3188	0.7	0.055
	$n_{\text{Ai}}^{T=0.001}$	104	1573	1615	3188	0.7	0.055

a smooth window-function trimming (of the function to be differentiated) near the boundary ($r > r_B = 0.75 \times B/2$) of the (large enough) numerical grid. This is already sufficient for selected systems like the noninteracting hydrogen atom in Fig. 1. We further regularize the partial derivatives at \mathbf{r} via convolution with a normal distribution centered at \mathbf{r} (using a standard deviation of $2a$ to $6a$ with lattice constant a). We then apply the same regularization to the gradient and the

Laplacian assembled from the regularized partial derivatives. This systematic approximation of the derivatives becomes increasingly accurate with rising spatial resolution.

3. Details on precision, accuracy, efficiency

The evaluation of the energy requires a high enough resolution of the integration grid. We obtain an estimate of the

TABLE IV. Details of the numerics pertinent to all electronic structure results from KS-DFT and DPFT presented in this work: The number G of grid points and the edge length L of the cubic numerical integration grid, as well as the corresponding resolution $L/\sqrt[3]{G}$. For the OF-DFT calculations with PROFESS, we chose 9000 eV (4000 eV) as the energy cutoff and an edge length of 15 Å (30 Å) with 240^3 (315^3) grid points for the atoms and dimers (the nanoparticle).

Figure	System	Density expression	Grid points	Edge length (Å)	Resolution (Å)
1	H	all	384^3	10	0.0260416
2	Al	all	256^3	12	0.046875
3	Mg	all	256^3	16	0.0625
4	Mg_2	n_{TF}	512^3	10	0.0195312
		$n_{3'}^T$	128^3	15	0.1171875
		$n_{3'}^F$	128^3	15	0.1171875
		n_{Ai}^T	512^3	16	0.03125
		KS	128^3	14.5	0.1132812
5	Al_2	$n_{\text{Ai}}^T(\mathcal{A})$ & KS	128^3	18	0.140625
		KS(\mathcal{A})	164^3	14.46421	0.0881964
		$n_{3'}^T$	192^3	18	0.09375
6	Al nanoparticle	n_{Ai}^T	384^3	36	0.09375
		$n_{3'}^T$	256^3	36	0.140625
		KS(384)	384^3	36	0.09375
		KS(256)	256^3	36	0.140625
7	Al nanoparticle	n_{Ai}^T	384^3	36	0.09375
		$n_{3'}^T$	256^3	36	0.140625
		KS	384^3	36	0.09375
8	Al nanoparticle	$n_{\text{Ai}}^T(\mathcal{A})$	384^3	36	0.09375
		KS(\mathcal{A})	384^3	30	0.078125
11	Mg_2	$n_{3'}^T$	128^3	15	0.1171875
		n_{Ai}^T	512^3	16	0.03125
		$n_{\text{Ai}}^T(\mathcal{A})$	384^3	36	0.09375

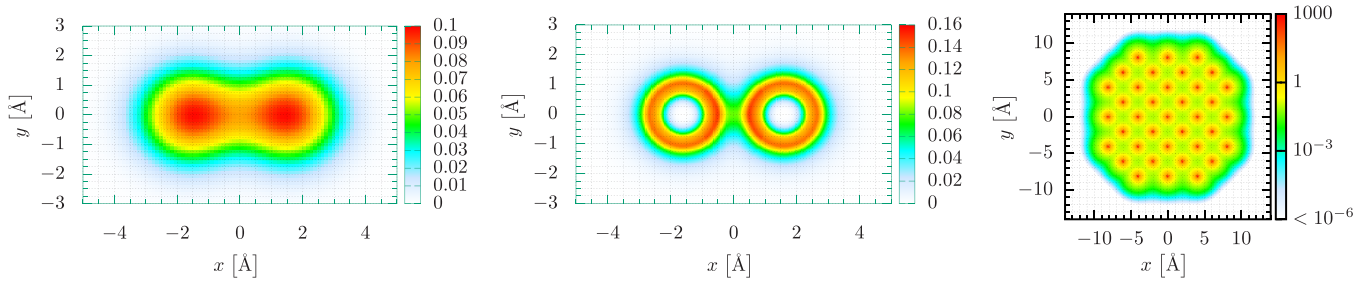


FIG. 11. The valence density contours $n_{3\gamma}^{T=0.4}$ (left) and $n_{Ai}^{T=0.1}$ (center) for the magnesium dimer of Fig. 4 and the all-electron density contour $n_{Ai}^{T=0.15}(\mathcal{E})$ (right) for the aluminum nanoparticle of Fig. 8. We display cuts in the plane of $z = 0$.

required grid size with setups for which we have an exact energy expression in terms of the particle density. In the case of hydrogen, we find a grid of $\sim 400^3$ points spaced at ~ 0.026 Å sufficient when evaluating the exact energy (in terms of the ground-state density) with the exact density (see Table I). Table II reports the self-consistent kinetic energies based on the semiclassical approximations $n_{3\gamma}$ and n_{Ai}^T for 384^3 grid points. In Fig. 9 we benchmark our DPFT densities against exact results for the three-dimensional isotropic harmonic oscillator. The TF densities capture the trend of the bulk (reasonably well for $N = 400$), but are of no use in the classically forbidden region. $n_{3\gamma}$ gives a rough average through the oscillations of the exact density and generates a decay into the classically forbidden region, albeit with too fat a tail and unphysical oscillations around zero. n_{Ai}^T performs best and yields a reasonable density profile even for $N = 1$. The exponential decay of its tail for $N = 400$ is close to the exact behavior, an observation that also holds for smaller N .

While the density profiles in Fig. 9 based on $n_{3\gamma}$ and, especially, n_{Ai}^T , present an enormous improvement over the TF densities, we gain little over the TF energies, which deviate by $\sim 1\%$ from the exact values, even as the particle number increases to $N = 400$ (see Table III). The high resolution suggested by the single-hydrogen atom for obtaining a precise semiclassical energy makes the energy evaluation for very inhomogeneous systems like nanoparticles a tedious undertaking. Indeed, our calculations do not indicate convergence of energies even when exceeding resolutions of 10 grid points

per angstrom for the 201-atom aluminum nanoparticle. We thus leave the precise and self-consistent determination of DPFT energies of chemical systems for future study. The integration grids for all computations presented in this work are listed in Table IV. In addition to the challenges in converging the DPFT energies, we also find them not accurate enough for chemistry applications that involve only a few electrons. We demonstrate this in the following by simulating the dissociation of the hydrogen molecule.

An almost ideal scenario in OF-DFT, maybe second to having the exact universal DFT functional, is to use a kinetic energy expression that is exact when evaluated with the exact density. This is of little value for DPFT calculations, whose defining feature is to avoid using the density functional $E_{kin}[n]$. However, while we have to live with an approximate interaction energy, we can evaluate the von Weizsäcker kinetic energy E_{kin}^{vW} , which is exact for the H_2 singlet ground state, with the converged self-consistent DPFT densities. This serves as a benchmarking exercise for the DPFT energies for small particle numbers N . Indeed, in Fig. 10 we show that $n_{3\gamma}$ delivers a qualitatively correct picture of the dissociation curve of the hydrogen molecule, which has been troubling generations of DFT practitioners [111–113]. While $n_{3\gamma}$ binds the two atoms, which improves qualitatively upon the TF model, the accuracy of the dissociation curve is lacking.

In Fig. 11 we show contour plots of electronic densities of the Mg dimer and the Al nanoparticle illustrated in Figs. 4 and 8, respectively.

-
- [1] P. Hohenberg and W. Kohn, Inhomogeneous electron gas, *Phys. Rev.* **136**, B864 (1964).
- [2] W. Kohn and L. J. Sham, Self-consistent equations including exchange and correlation effects, *Phys. Rev.* **140**, A1133 (1965).
- [3] K. Burke, Perspective on density functional theory, *J. Chem. Phys.* **136**, 150901 (2012).
- [4] A. D. Becke, Perspective: Fifty years of density-functional theory in chemical physics, *J. Chem. Phys.* **140**, 18A301 (2014).
- [5] P. J. Hasnip, K. Refson, M. I. J. Probert, J. R. Yates, S. J. Clark, and C. J. Pickard, Density functional theory in the solid state, *Philos. Trans. R. Soc. A* **372**, 20130270 (2014).
- [6] B. Kalita, L. Li, R. J. McCarty, and K. Burke, Learning to approximate density functionals, *Acc. Chem. Res.* **54**, 818 (2021).
- [7] J. M. Soler, E. Artacho, J. D. Gale, A. García, J. Junquera, P. Ordejón, and D. Sánchez-Portal, The SIESTA method for ab initio order-N materials simulation, *J. Phys.: Condens. Matter* **14**, 2745 (2002).
- [8] D. Bowler and T. Miyazaki, O(N) methods in electronic structure calculations, *Rep. Prog. Phys.* **75**, 036503 (2012).
- [9] S. Mohr, L. E. Ratcliff, L. Genovese, D. Caliste, P. Boulanger, S. Goedecker, and T. Deutsch, Accurate and efficient linear scaling DFT calculations with universal applicability, *Phys. Chem. Chem. Phys.* **17**, 31360 (2015).
- [10] D. J. Cole and N. D. M. Hine, Applications of large-scale density functional theory in biology, *J. Phys.: Condens. Matter* **28**, 393001 (2016).
- [11] A. Nakata, J. S. Baker, S. Y. Mujahed, J. T. L. Poulton, S. Arapan, J. Lin, Z. Raza, S. Yadav, L. Truffandier, T. Miyazaki,

- and D. R. Bowler, Large scale and linear scaling DFT with the CONQUEST code, *J. Chem. Phys.* **152**, 164112 (2020).
- [12] J. C. A. Prentice, J. Aarons, J. C. Womack, A. E. A. Allen, L. Andrinopoulos, L. Anton, R. A. Bell, A. Bhandari, G. A. Bramley, R. J. Charlton *et al.*, The ONETEP linear-scaling density functional theory program, *J. Chem. Phys.* **152**, 174111 (2020).
- [13] J. Aarons, M. Sarwar, D. Thompsett, and C.-K. Skylaris, Perspective: Methods for large-scale density functional calculations on metallic systems, *J. Chem. Phys.* **145**, 220901 (2016).
- [14] M. Chen, X.-W. Jiang, H. Zhuang, L.-W. Wang, and E. A. Carter, Petascale orbital-free density functional theory enabled by small-box algorithms, *J. Chem. Theory Comput.* **12**, 2950 (2016).
- [15] W. C. Witt, B. G. del Rio, J. M. Dieterich, and E. A. Carter, Orbital-free density functional theory for materials research, *J. Mater. Res.* **33**, 777 (2018).
- [16] M. Elstner and G. Seifert, Density functional tight binding, *Philos. Trans. R. Soc. A* **372**, 20120483 (2014).
- [17] P. Golub and S. Manzhos, Kinetic energy densities based on the fourth order gradient expansion: performance in different classes of materials and improvement via machine learning, *Phys. Chem. Chem. Phys.* **21**, 378 (2019).
- [18] M. Fujinami, R. Kageyama, J. Seino, Y. Ikabata, and H. Nakai, Orbital-free density functional theory calculation applying semi-local machine-learned kinetic energy density functional and kinetic potential, *Chem. Phys. Lett.* **748**, 137358 (2020).
- [19] S. Manzhos and P. Golub, Data-driven kinetic energy density fitting for orbital-free DFT: Linear vs Gaussian process regression, *J. Chem. Phys.* **153**, 074104 (2020).
- [20] J. Lüder and S. Manzhos, Nonparametric local pseudopotentials with machine learning: A tin pseudopotential built using gaussian process regression, *J. Phys. Chem. A* **124**, 11111 (2020).
- [21] C. W. Tan, C. J. Pickard, and W. C. Witt, Automatic differentiation for orbital-free density functional theory, *J. Chem. Phys.* **158**, 124801 (2023).
- [22] W. C. Witt and E. A. Carter, Kinetic energy density of nearly free electrons. I. Response functionals of the external potential, *Phys. Rev. B* **100**, 125106 (2019).
- [23] W. C. Witt and E. A. Carter, Kinetic energy density of nearly free electrons. II. Response functionals of the electron density, *Phys. Rev. B* **100**, 125107 (2019).
- [24] W. C. Witt, K. Jiang, and E. A. Carter, Upper bound to the gradient-based kinetic energy density of noninteracting electrons in an external potential, *J. Chem. Phys.* **151**, 064113 (2019).
- [25] X. Shao, K. Jiang, W. Mi, A. Genova, and M. Pavanello, DFTpy: An efficient and object-oriented platform for orbital-free DFT simulations, *Wiley Interdiscip. Rev. Comput. Mol. Sci.* **11**, e1482 (2021).
- [26] K. Jiang and M. Pavanello, Time-dependent orbital-free density functional theory: Background and Pauli kernel approximations, *Phys. Rev. B* **103**, 245102 (2021).
- [27] K. Jiang, X. Shao, and M. Pavanello, Efficient time-dependent orbital-free density functional theory: Semilocal adiabatic response, *Phys. Rev. B* **106**, 115153 (2022).
- [28] F. Della Sala, Orbital-free methods for plasmonics: Linear response, *J. Chem. Phys.* **157**, 104101 (2022).
- [29] Q. Xu, C. Ma, W. Mi, Y. Wang, and Y. Ma, Nonlocal pseudopotential energy density functional for orbital-free density functional theory, *Nat. Commun.* **13**, 1385 (2022).
- [30] J. P. Perdew, K. Burke, and M. Ernzerhof, Generalized gradient approximation made simple, *Phys. Rev. Lett.* **77**, 3865 (1996).
- [31] J. P. Perdew, K. Burke, and M. Ernzerhof, Generalized gradient approximation made simple [Phys. Rev. Lett. 77, 3865 (1996)], *Phys. Rev. Lett.* **78**, 1396(E) (1997).
- [32] J. G. Vilhena, E. Räsänen, M. A. L. Marques, and S. Pittalis, Construction of the B88 exchange-energy functional in two dimensions, *J. Chem. Theory Comput.* **10**, 1837 (2014).
- [33] R. F. Ribeiro, D. Lee, A. Cangi, P. Elliott, and K. Burke, Corrections to Thomas–Fermi densities at turning points and beyond, *Phys. Rev. Lett.* **114**, 050401 (2015).
- [34] P. Okun and K. Burke, Semiclassics: The hidden theory behind the success of DFT in *Density Functionals for Many-Particle Systems: Mathematical Theory and Physical Applications of Effective Equations*, edited by B.-G. Englert, H. Siedentop, and M.-I. Trappe, Lecture Notes Series, IMS (World Scientific, Singapore, 2023), pp. 179–249.
- [35] P. N. Ma, S. Pilati, M. Troyer, and X. Dai, Density functional theory for atomic Fermi gases, *Nat. Phys.* **8**, 601 (2012).
- [36] M.-I. Trappe, Y. L. Len, H. K. Ng, C. A. Müller, and B.-G. Englert, Leading gradient correction to the kinetic energy for two-dimensional fermion gases, *Phys. Rev. A* **93**, 042510 (2016).
- [37] M. I. Trappe, Y. L. Len, H. K. Ng, and B. G. Englert, Airy-averaged gradient corrections for two-dimensional fermion gases, *Ann. Phys. (NY)* **385**, 136 (2017).
- [38] M.-I. Trappe, P. T. Grochowski, J. H. Hue, T. Karpiuk, and K. Rzażewski, Phase transitions of repulsive two-component fermi gases in two dimensions, *New J. Phys.* **23**, 103042 (2021).
- [39] Q. Xu, J. Lv, Y. Wang, and Y. Ma, Nonlocal kinetic energy density functionals for isolated systems obtained via local density approximation kernels, *Phys. Rev. B* **101**, 045110 (2020).
- [40] J. Lehtomäki, I. Makkonen, M. A. Caro, A. Harju, and O. Lopez-Acevedo, Orbital-free density functional theory implementation with the projector augmented-wave method, *J. Chem. Phys.* **141**, 234102 (2014).
- [41] M. Chen, J. Xia, C. Huang, J. M. Dieterich, L. Hung, I. Shin, and E. A. Carter, Introducing PROFESS 3.0: An advanced program for orbital-free density functional theory molecular dynamics simulations, *Comput. Phys. Commun.* **190**, 228 (2015).
- [42] J. M. Dieterich, W. C. Witt, and E. A. Carter, libKEDF: An accelerated library of kinetic energy density functionals, *J. Comput. Chem.* **38**, 1552 (2017).
- [43] W. Mi, X. Shao, C. Su, Y. Zhou, S. Zhang, Q. Li, H. Wang, L. Zhang, M. Miao, Y. Wang, and Y. Ma, ATLAS: A real-space finite-difference implementation of orbital-free density functional theory, *Comput. Phys. Commun.* **200**, 87 (2016).
- [44] X. Shao, Q. Xu, S. Wang, J. Lv, Y. Wang, and Y. Ma, Large-scale ab initio simulations for periodic system, *Comput. Phys. Commun.* **233**, 78 (2018).
- [45] P. Golub and S. Manzhos, CONUNDrum: A program for orbital-free density functional theory calculations, *Comput. Phys. Commun.* **256**, 107365 (2020).

- [46] L.-W. Wang and M. P. Teter, Kinetic-energy functional of the electron density, *Phys. Rev. B* **45**, 13196 (1992).
- [47] Y. A. Wang, N. Govind, and E. A. Carter, Orbital-free kinetic-energy functionals for the nearly free electron gas, *Phys. Rev. B* **58**, 13465 (1998).
- [48] Y. A. Wang, N. Govind, and E. A. Carter, Orbital-free kinetic-energy density functionals with a density-dependent kernel, *Phys. Rev. B* **60**, 16350 (1999).
- [49] C. Huang and E. A. Carter, Nonlocal orbital-free kinetic energy density functional for semiconductors, *Phys. Rev. B* **81**, 045206 (2010).
- [50] L. A. Constantin, E. Fabiano, and F. Della Sala, Performance of semilocal kinetic energy functionals for orbital-free density functional theory, *J. Chem. Theory Comput.* **15**, 3044 (2019).
- [51] D. R. Murphy, Sixth-order term of the gradient expansion of the kinetic-energy density functional, *Phys. Rev. A* **24**, 1682 (1981).
- [52] W. Yang, Gradient correction in Thomas–Fermi theory, *Phys. Rev. A* **34**, 4575 (1986).
- [53] R. M. Dreizler and E. K. U. Gross, *Density Functional Theory* (Springer, Berlin, 1990).
- [54] A. Sergeev, R. Jovanovic, S. Kais, and F. H. Alharbi, On the divergence of gradient expansions for kinetic energy functionals in the potential functional theory, *J. Phys. A: Math. Theor.* **49**, 285202 (2016).
- [55] K. Luo, V. V. Karasiev, and S. B. Trickey, A simple generalized gradient approximation for the noninteracting kinetic energy density functional, *Phys. Rev. B* **98**, 041111(R) (2018).
- [56] L. A. Constantin, E. Fabiano, and F. Della Sala, Semilocal pauli–gaussian kinetic functionals for orbital-free density functional theory calculations of solids, *J. Phys. Chem. Lett.* **9**, 4385 (2018).
- [57] L. A. Constantin, E. Fabiano, and F. Della Sala, Modified fourth-order kinetic energy gradient expansion with hartree potential-dependent coefficients, *J. Chem. Theory Comput.* **13**, 4228 (2017).
- [58] L. A. Espinosa Leal, A. Karpenko, M. A. Caro, and O. Lopez-Acevedo, Optimizing a parametrized Thomas–Fermi–Dirac–Weizsäcker density functional for atoms, *Phys. Chem. Chem. Phys.* **17**, 31463 (2015).
- [59] D. García-Aldea and J. E. Alvarillos, Generalized nonlocal kinetic energy density functionals based on the von Weizsäcker functional, *Phys. Chem. Chem. Phys.* **14**, 1756 (2012).
- [60] V. V. Karasiev, D. Chakraborty, O. A. Shukruto, and S. B. Trickey, Nonempirical generalized gradient approximation free-energy functional for orbital-free simulations, *Phys. Rev. B* **88**, 161108(R) (2013).
- [61] D. García-Aldea and J. E. Alvarillos, Kinetic-energy density functionals with nonlocal terms with the structure of the Thomas–Fermi functional, *Phys. Rev. A* **76**, 052504 (2007).
- [62] W. Mi, A. Genova, and M. Pavanello, Nonlocal kinetic energy functionals by functional integration, *J. Chem. Phys.* **148**, 184107 (2018).
- [63] D. Chakraborty, R. Cuevas-Saavedra, and P. W. Ayers, Two-point weighted density approximations for the kinetic energy density functional, *Theor. Chem. Acc.* **136**, 113 (2017).
- [64] K. Yao and J. Parkhill, Kinetic energy of hydrocarbons as a function of electron density and convolutional neural networks, *J. Chem. Theory Comput.* **12**, 1139 (2016).
- [65] O. A. von Lilienfeld and K. Burke, Retrospective on a decade of machine learning for chemical discovery, *Nat. Commun.* **11**, 4895 (2020).
- [66] J. Westermayr, M. Gastegger, K. T. Schütt, and R. J. Maurer, Perspective on integrating machine learning into computational chemistry and materials science, *J. Chem. Phys.* **154**, 230903 (2021).
- [67] W. Yang, P. W. Ayers, and Q. Wu, Potential functionals: Dual to density functionals and solution to the v -representability problem, *Phys. Rev. Lett.* **92**, 146404 (2004).
- [68] A. Cangi, E. K. U. Gross, and K. Burke, Potential functionals versus density functionals, *Phys. Rev. A* **88**, 062505 (2013).
- [69] D. Peng, B. Zhao, A. J. Cohen, X. Hu, and W. Yang, Optimized effective potential for calculations with orbital-free potential functionals, *Mol. Phys.* **110**, 925 (2012).
- [70] P. Elliott, A. Cangi, S. Pittalis, E. K. U. Gross, and K. Burke, Almost exact exchange at almost no computational cost in electronic structure, *Phys. Rev. A* **92**, 022513 (2015).
- [71] B.-G. Englert and J. Schwinger, Thomas–Fermi revisited: The outer regions of the atom, *Phys. Rev. A* **26**, 2322 (1982).
- [72] B.-G. Englert and J. Schwinger, Statistical atom: Handling the strongly bound electrons, *Phys. Rev. A* **29**, 2331 (1984).
- [73] B.-G. Englert and J. Schwinger, Statistical atom: Some quantum improvements, *Phys. Rev. A* **29**, 2339 (1984).
- [74] B.-G. Englert and J. Schwinger, New statistical atom: A numerical study, *Phys. Rev. A* **29**, 2353 (1984).
- [75] B.-G. Englert and J. Schwinger, Semiclassical atom, *Phys. Rev. A* **32**, 26 (1985).
- [76] B.-G. Englert and J. Schwinger, Atomic-binding-energy oscillations, *Phys. Rev. A* **32**, 47 (1985).
- [77] B.-G. Englert, *Semiclassical Theory of Atoms*, Lecture Notes in Physics (Springer, Berlin, 1988).
- [78] M. Cinal and B.-G. Englert, Thomas–Fermi–Scott model in momentum space, *Phys. Rev. A* **45**, 135 (1992).
- [79] B.-G. Englert, Energy functionals and the Thomas–Fermi model in momentum space, *Phys. Rev. A* **45**, 127 (1992).
- [80] M. Cinal and B.-G. Englert, Energy functionals in momentum space: Exchange energy, quantum corrections, and the Kohn–Sham scheme, *Phys. Rev. A* **48**, 1893 (1993).
- [81] B.-G. Englert, Julian Schwinger and the Semiclassical Atom, in *Proceedings of the Julian Schwinger Centennial Conference*, edited by B.-G. Englert (World Scientific, Singapore, 2019), Chap. 17, pp. 261–269.
- [82] T. T. Chau, J. H. Hue, M.-I. Trappe, and B.-G. Englert, Systematic corrections to the Thomas–Fermi approximation without a gradient expansion, *New J. Phys.* **20**, 073003 (2018).
- [83] M.-I. Trappe, J. H. Hue, and B.-G. Englert, Density-potential functional theory for fermions in one dimension, in *Density Functionals for Many-Particle Systems: Mathematical Theory and Physical Applications of Effective Equations*, edited by B.-G. Englert, H. Siedentop, and M.-I. Trappe, Lecture Notes Series, IMS (World Scientific, Singapore, 2023), pp. 251–267.
- [84] M.-I. Trappe, D. Y. H. Ho, and S. Adam, First-principles quantum corrections for carrier correlations in double-layer two-dimensional heterostructures, *Phys. Rev. B* **99**, 235415 (2019).
- [85] J. H. Hue, Orbital-free density functionals for fermion gases, Ph.D. thesis, National University of Singapore, Singapore, 2020.

- [86] M.-I. Trappe and R. A. Chisholm, A density functional theory for ecology across scales, *Nat. Commun.* **14**, 1089 (2023).
- [87] M. G. Medvedev, I. S. Bushmarinov, J. Sun, J. P. Perdew, and K. A. Lyssenko, Density functional theory is straying from the path toward the exact functional, *Science* **355**, 49 (2017).
- [88] X. Lan, S. Masala, and E. H. Sargent, Charge-extraction strategies for colloidal quantum dot photovoltaics, *Nat. Mater.* **13**, 233 (2014).
- [89] E. C. Tyo and S. Vajda, Catalysis by clusters with precise numbers of atoms, *Nat. Nanotechnol.* **10**, 577 (2015).
- [90] Y. Attia and M. Samer, Metal clusters: New era of hydrogen production, *Renewable and Sustainable Energy Rev.* **79**, 878 (2017).
- [91] M. Jäger, R. Schäfer, and R. L. Johnston, First principles global optimization of metal clusters and nanoalloys, *Adv. Phys.: X* **3**, 1516514 (2018).
- [92] Y. Hui, X. Yi, F. Hou, D. Wibowo, F. Zhang, D. Zhao, H. Gao, and C.-X. Zhao, Role of nanoparticle mechanical properties in cancer drug delivery, *ACS Nano* **13**, 7410 (2019).
- [93] W. Mi and M. Pavanello, Orbital-free density functional theory correctly models quantum dots when asymptotics, nonlocality, and nonhomogeneity are accounted for, *Phys. Rev. B* **100**, 041105(R) (2019).
- [94] H. Do and N. A. Besley, Structural optimization of molecular clusters with density functional theory combined with basin hopping, *J. Chem. Phys.* **137**, 134106 (2012).
- [95] J. Cuny, N. Tarrat, F. Spiegelman, A. Huguenot, and M. Rapacioli, Density-functional tight-binding approach for metal clusters, nanoparticles, surfaces and bulk: Application to silver and gold, *J. Phys.: Condens. Matter* **30**, 303001 (2018).
- [96] S. Lysgaard, J. S. G. Mýrdal, H. A. Hansen, and T. Vegge, A DFT-based genetic algorithm search for AuCu nanoalloy electrocatalysts for CO₂ reduction, *Phys. Chem. Chem. Phys.* **17**, 28270 (2015).
- [97] X. Shao, W. Mi, and M. Pavanello, Efficient DFT solver for nanoscale simulations and beyond, *J. Phys. Chem. Lett.* **12**, 4134 (2021).
- [98] K. Buchwald and B.-G. Englert, Thomas–Fermi–Scott model: Momentum-space density, *Phys. Rev. A* **40**, 2738 (1989).
- [99] B.-G. Englert, J. H. Hue, Z. C. Huang, M. M. Paraniak, and M.-I. Trappe, Energy functionals of single-particle densities: A unified view, in *Density Functionals for Many-Particle Systems: Mathematical Theory and Physical Applications of Effective Equations*, edited by B.-G. Englert, H. Siedentop, and M.-I. Trappe, Lecture Notes Series, IMS (World Scientific, Singapore, 2023), pp. 287–308.
- [100] M.-I. Trappe, J. H. Hue, J. Z. C. Huang, M. Paraniak, D. Hiller, J. Ciosłowski, and B.-G. Englert, Single-particle-exact density functional theory, *Ann. Phys.* **459**, 169497 (2023).
- [101] C. E. González-Espinoza, P. W. Ayers, J. Karwowski, and A. Savin, Smooth models for the Coulomb potential, *Theor. Chem. Acc.* **135**, 256 (2016).
- [102] F. Gygi, All-electron plane-wave electronic structure calculations, *J. Chem. Theory Comput.* **19**, 1300 (2023).
- [103] S. H. Vosko, L. Wilk, and M. Nusai, Accurate spin-dependent electron liquid correlation energies for local spin density calculations: a critical analysis, *Can. J. Phys.* **58**, 1200 (1980).
- [104] S. Lehtola, C. Steigemann, M. J. Oliveira, and M. A. Marques, Recent developments in libxc—A comprehensive library of functionals for density functional theory, *SoftwareX* **7**, 1 (2018).
- [105] M. J. Frisch, G. W. Trucks, H. B. Schlegel, G. E. Scuseria, M. A. Robb, J. R. Cheeseman, G. Scalmani, V. Barone, G. A. Petersson, H. Nakatsuji *et al.*, *Gaussian 16 Revision C.01* Gaussian Inc. Wallingford, CT, 2016).
- [106] X. Gonze, B. Amadon, G. Antonius, F. Arnardi, L. Baguet, J.-M. Beuken, J. Bieder, F. Bottin, J. Bouchet, E. Bousquet *et al.*, The Abinit project: Impact, environment and recent developments, *Comput. Phys. Commun.* **248**, 107042 (2020).
- [107] J. C. Slater, *The Self-Consistent Field for Molecular and Solids*, Quantum Theory of Molecular and Solids, Vol. 4 (McGraw-Hill, New York, 1974).
- [108] C. Huang and E. A. Carter, Transferable local pseudopotentials for magnesium, aluminum and silicon, *Phys. Chem. Chem. Phys.* **10**, 7109 (2008).
- [109] F. Legrain and S. Manzhos, Highly accurate local pseudopotentials of Li, Na, and Mg for orbital free density functional theory, *Chem. Phys. Lett.* **622**, 99 (2015).
- [110] M. Frigo and S. G. Johnson, The Design and Implementation of FFTW3, *Proc. IEEE* **93**, 216 (2005).
- [111] A. J. Cohen, P. Mori-Sánchez, and W. Yang, Insights into current limitations of density functional theory, *Science* **321**, 792 (2008).
- [112] S. Vuckovic, T. J. P. Irons, L. O. Wagner, A. M. Teale, and P. Gori-Giorgi, Interpolated energy densities, correlation indicators and lower bounds from approximations to the strong coupling limit of DFT, *Phys. Chem. Chem. Phys.* **19**, 6169 (2017).
- [113] D. Zhang and D. G. Truhlar, Unmasking static correlation error in hybrid kohn–sham density functional theory, *J. Chem. Theory Comput.* **16**, 5432 (2020).
- [114] M. Brack and B. P. van Zyl, Simple analytical particle and kinetic energy densities for a dilute fermionic gas in a d-dimensional harmonic trap, *Phys. Rev. Lett.* **86**, 1574 (2001).